Structures 80 (2025) 109902



Contents lists available at ScienceDirect

Structures

journal homepage: www.elsevier.com/locate/structures



Importance of specimen size effect for AAC infill walls in ASTM E519 diagonal shear test

Nilay Sabahoğlu [a], Muhammet Musab Erdem [a], Engin Emsen [b], Murat Bikçe [a,*]

[a] Department of Civil Engineering, Faculty of Engineering and Natural Sciences, Iskenderun Technical University, Hatay 31200, Turkey
[b] Department of Civil Engineering, Faculty of Engineering, Akdeniz University, Antalya 07070, Turkey

ARTICLE INFO

Keywords:
ASTM E519
Diagonal shear test
Autoclaved aerated concrete (AAC)
Infill wall
Specimen size effect
Numerical analysis

ABSTRACT

Accurate estimation of the shear strength of masonry and infill walls is crucial for evaluating the seismic performance of structures. According to ASTM E519, specimens with minimum dimensions of 120 × 120 cm are recommended to determine the shear strength of these walls. However, many studies employ smaller specimens due to practical limitations such as cost, workmanship, ease of application, and laboratory constraints. Recent studies (e.g., Dorji et al., 2022; Gupta et al., 2023) emphasize the need for further experimental data to assess how specimen size affects measured shear strength. In response to this requirement, the present study investigates the influence of reduced-size specimens on the shear strength of Autoclaved Aerated Concrete (AAC) masonry walls through experimental testing. AAC blocks, widely preferred for their thermal insulation, fire resistance, ease of handling, and low density, were used as the unit material. Experimental results show that smaller specimens tend to exhibit higher shear strengths than the standard-sized ones, and these findings are presented graphically. Furthermore, a conversion equation is proposed to estimate the shear strength of standard-sized specimens based on the observed trends. Finally, complementary numerical analyses were conducted to support the experimental results and to evaluate intermediate and larger specimen sizes that could not be tested in the laboratory.

1. Introduction

In masonry structures, horizontal and vertical loads are carried by the load-bearing walls. On the other hand, the resistance of infill walls against these loads is theoretically neglected in reinforced concrete structures. However, the behavior of the structure under seismic loads can be affected by these walls in a positive or negative way. Studies have shown that infill walls, due to their in-plane stiffness, react to lateral loading and significantly affect the behavior of frame [1–22]. In these studies, it is stated that the presence of infill walls increases lateral stiffness, load carrying capacity, energy dissipation and reduces the natural vibration period of the system. The absence of infill walls in the building's design or their incorrect modeling has a significant impact on the structure's seismic performance [23]. The accuracy of the shear strength selected for the wall is very important in predicting the infill wall behavior under horizontal action [24]. In this direction, the accuracy of the analysis results obtained in the design of new structures or in the evaluation and retrofitting of existing structures depends on the determination of the wall mechanical properties in accordance with the actual behavior [24,25]. The best understanding of the structural behavior is only possible if the mechanical properties and in-plane shear strength of the load-bearing and non-load-bearing infill walls are correctly defined in the numerical model. During seismic actions, infill walls are subjected to various damages dominated by diagonal shear cracking due to their brittle nature [26,27]. One of the main methods used to obtain the shear strength of walls is the 'Diagonal Shear Test' method. To determine this strength, the test method prepared by the American Society for Testing Materials (ASTM) and the details of which are presented in code E519/E519M [28] is generally used. This test method involves determination of the diagonal tensile or shear strength of wall assemblies loaded under compression along a diagonal. In the test, a diagonal stress fracture occurs by separating the specimen parallel to the load direction [29].

According to ASTM E519, diagonal shear strength is determined by wall specimens with a minimum size of 120 × 120 cm. This recommendation is made for reasons such as being able to adequately

* Corresponding author.
E-mail addresses: sabahoglunilay@gmail.com (N. Sabahoğlu), musab.erdem@iste.edu.tr (M.M. Erdem), eemsen@akdeniz.edu.tr (E. Emsen), murat.bikce@iste.edu.tr (M. Bikçe).

https://doi.org/10.1016/j.istruc.2025.109902
Received 15 March 2025; Received in revised form 30 June 2025; Accepted 6 August 2025
Available online 16 August 2025
2352-0124/© 2025 Institution of Structural Engineers. Published by Elsevier Ltd. All rights are reserved, including those for text and data mining, AI training, and similar technologies.

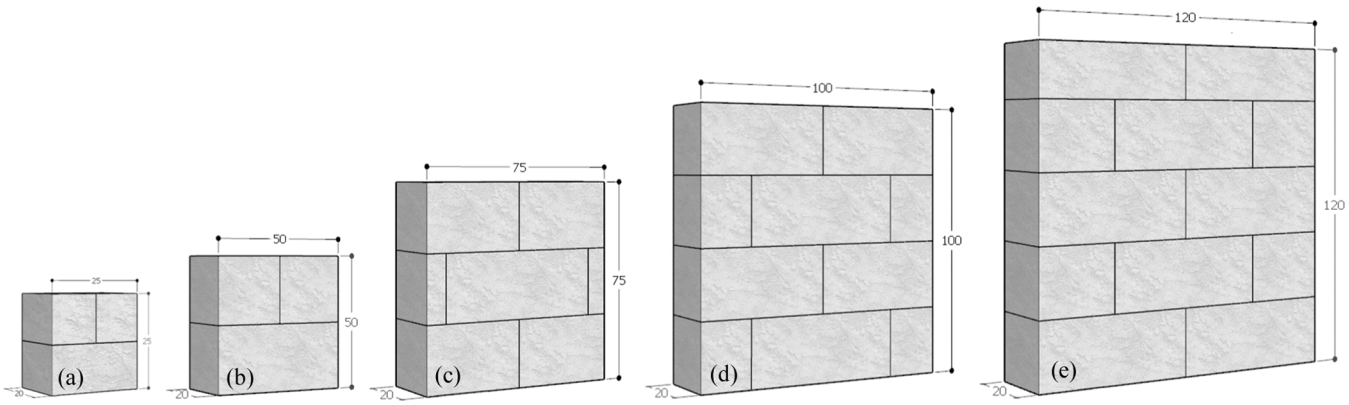


Fig. 1. Wall specimens (a) 25 × 25 × 20; (b) 50 × 50 × 20; (c) 75 × 75 × 20; (d) 100 × 100 × 20; (e) 120 × 120 × 20 "cm".

represent a real wall and to ensure compatibility many laboratories test equipment [30]. The ASTM E519 standard provides for the use of small-sized specimens in comparative studies of variables affecting the behavior of infill walls. However, a correlation to adapt the test results obtained from small specimens to the standard wall dimensions has not been presented in ASTM E519. In literature, studies in which small size specimens have been preferred due to reasons such as cost, workmanship, ease of application, and laboratory facilities are frequently encountered [18,31–41]. For example; Ferretti et al. [25] carried out their experiments on the mechanical characterization of AAC wall panels on 75 × 62.5, 75 × 60 and 25 × 25 cm, Kanchidurai et al. [42] conducted their research on the shear strength of brick wall panels on 48 × 48 cm, Kubica and Galman [43] carried out their AAC infill wall experiments on 80 × 90 cm, Silva et al. [44] used specimens of 75 × 75 cm and 83 × 83 cm for their hollow brick experiments. Yardım and Lalaj [45] performed diagonal shear tests in accordance with ASTM E519 standard for a total of 12 wall specimens of two different sizes, 2 full-scale specimens of 120 × 120 × 25 cm and 10 half-scale specimens of 65 × 65 × 25 cm, in their experimental study for strengthening walls with brick unit elements. Basha and Kaushik [27] tested 10 full-scale brick wall specimens of 120 × 120 × 11 cm and 10 half-scale brick wall specimens of 60 × 60 × 11 cm to evaluate the effect of wall specimen size on diagonal shear strength. Ozsayin et al. [46] conducted tests on 36 hollow brick wall specimens subjected to both uniaxial compression and diagonal tension loading, carried out before and after the external retrofitting using CFRP sheets. The experimental variables included wall dimensions, brick hole orientation, mortar type, the quantity of CFRP reinforcement, and specific details of the strengthening methodology. In the study, considering parametric variables such as wall dimensions, mortar type and reinforcement sheets, smaller specially produced hollow bricks were used by scaling the width, height and thickness dimensions of the standard brick block by 1/3. All the 24 wall specimens of 35 × 35 × 7 cm and 50 × 50 × 7 cm were produced with these bricks and diagonal shear tests were performed on the specimens in accordance with ASTM E519.

On the other hand, Thatikonda, N.P. et al. [47] state that various difficulties may arise during the transportation and testing of historical wall samples due to the quasi-brittle material behavior of wall components, and that many authors have recognized these problems and made changes to the test rules by modifying the sample and load orientation, or by proposing specimens with a reduced scale. Furthermore, the researchers highlighted the size effect in their studies and stating that the findings of small specimens should not be directly generalized to large panels when deviating from the ASTM E519 standard.

As a comprehensive study on the size effect in the literature, Lim [48] examined how the size of masonry brick walls affects their shear strength and behavior under diagonal compression. The study tested 60 unreinforced concrete brick wall panels of two different sizes using five different mortar mix ratios. The results showed that larger wall panels exhibited lower shear strength in diagonal tension failure, confirming a size effect only for this specific failure mode. Depending on the mortar-to-brick strength ratio, various failure modes were observed, including diagonal tension, toe crushing, sliding, and combined failures. The test results revealed a correlation between diagonal tension strength and wall size. The paper also presents a regression-based equation for predicting diagonal tension strength as a function of wall height. This equation could be useful for structural code comparisons and masonry design. Considering the studies mentioned above, it has been realized that when the tested wall specimen size is smaller than the size required by the standard, the mean failure load is obtained at a higher value than it should be and hence the mean shear strength also increased.

Bearing or non-bearing infill walls can be made of different materials such as stone, brick, briquette, autoclaved aerated concrete (AAC) or adobe. In this study, in order to examine the effect of using small sized specimens on shear strength, three AAC infill wall specimens of five different sizes, 25 × 25, 50 × 50, 75 × 75, 100 × 100, and 120 × 120 cm, with a constant thickness of 20 cm, were tested. Specimen dimensions were determined in accordance with commonly encountered practices in literature. Additionally, the dimensions were systematically reduced to establish a reliable trend line for shear strength variation. AAC blocks widely used in terms of thermal insulation, fire resistance, formability and lightness were preferred as unit material in the experiments [13,14,18,34,35,49–54]. The shear strengths obtained experimentally from small specimens are compared with the 120 × 120 cm specimens recommended by ASTM E519. In this research, it has been understood that the shear strengths obtained from small specimen sizes are higher than the values obtained from the sizes recommended by ASTM E519. It is determined that it would be useful to consider this situation in future academic studies.

In recent decades, several numerical modelling strategies, which capable of representing the motion of multiple and intersecting units explicitly, have become increasingly popular for the structural and seismic assessment of unreinforced masonry structures [55]. In addition to experimental work, numerical analyses were conducted to support the findings of this study. Intermediate and large-sized specimens that could not be tested experimentally were also considered as numerical models. To achieve this, a simplified micro-modeling approach was adopted to simulate specified experimental behavior.

2. Production of specimens

All dimensions specified in this study are "Width×Height×Thickness", respectively (Fig. 1a-e). Since the wall specimens had square dimensions and thickness is kept constant at 20 cm, the experimental group names are expressed as 25 × 25, 50 × 50, 75 × 75, 100 × 100, and 120 × 120 cm. In this study, the definition as 25–1 represents the first

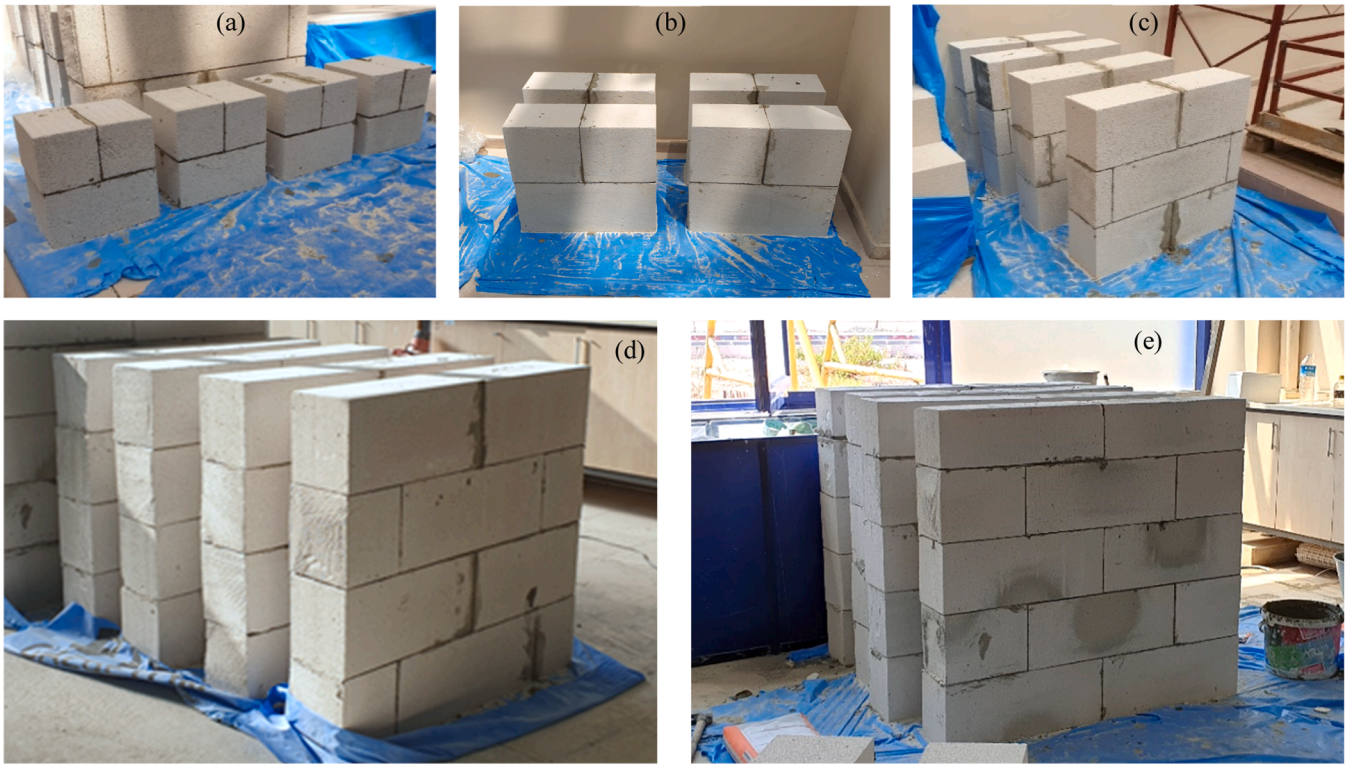


Fig. 2. Produced wall specimens (a) 25 × 25 × 20; (b) 50 × 50 × 20; (c) 75 × 75 × 20; (d) 100 × 100 × 20; (e) 120 × 120 × 20 "cm".

Table 1
Compression test for AAC units (10 ×10 ×10 cm).

	Failure pattern	Failure load (kN)	Compressive strength (MPa)	Avg. comp. strength (MPa)
1		16.14	1.61	
2		18.07	1.81	
				1.86
3		20.24	2.02	
4		19.80	1.98	

specimen with dimensions of 25 × 25 × 20 cm.

Although 4 wall specimens were prepared for each experimental group of varied sizes, 3 wall specimens were subjected to diagonal shear test. One extra specimen for each group was kept ready as a reserve for possible problems that may occur during transport, placement or testing. For this reason, a total of 15 specimens, 3 in each experimental group, were subjected to the test and the results obtained are evaluated. In all wall specimens, AAC units with dimensions of 60 × 25 × 20 cm were cut with a saw to the specified dimensions and the joints between the units were bonded with commonly used grout.

Michelini et al. [34] present an experimental investigation on the shear behavior of Autoclaved Aerated Concrete (AAC) masonry, focusing on the influence of block density, mortar type, and testing setup. The study examined two block densities (300 and 480 kg/m^3) and two thin-layer mortars (one commercial PM-TLM, and one alkali-activated AA-TLM). The analysis involved a series of tests,

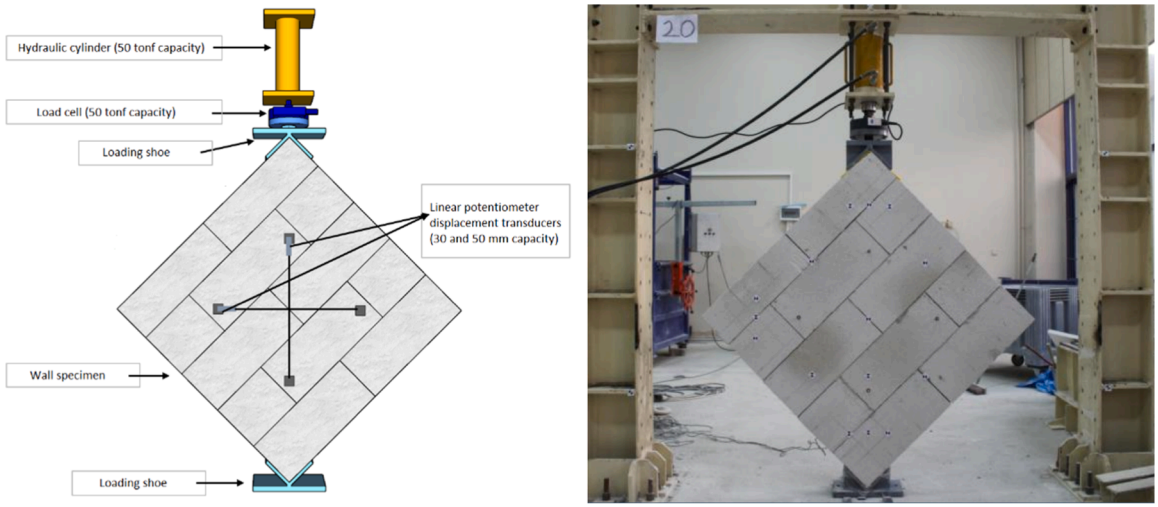


Fig. 3. Wall specimen and measurement setup.

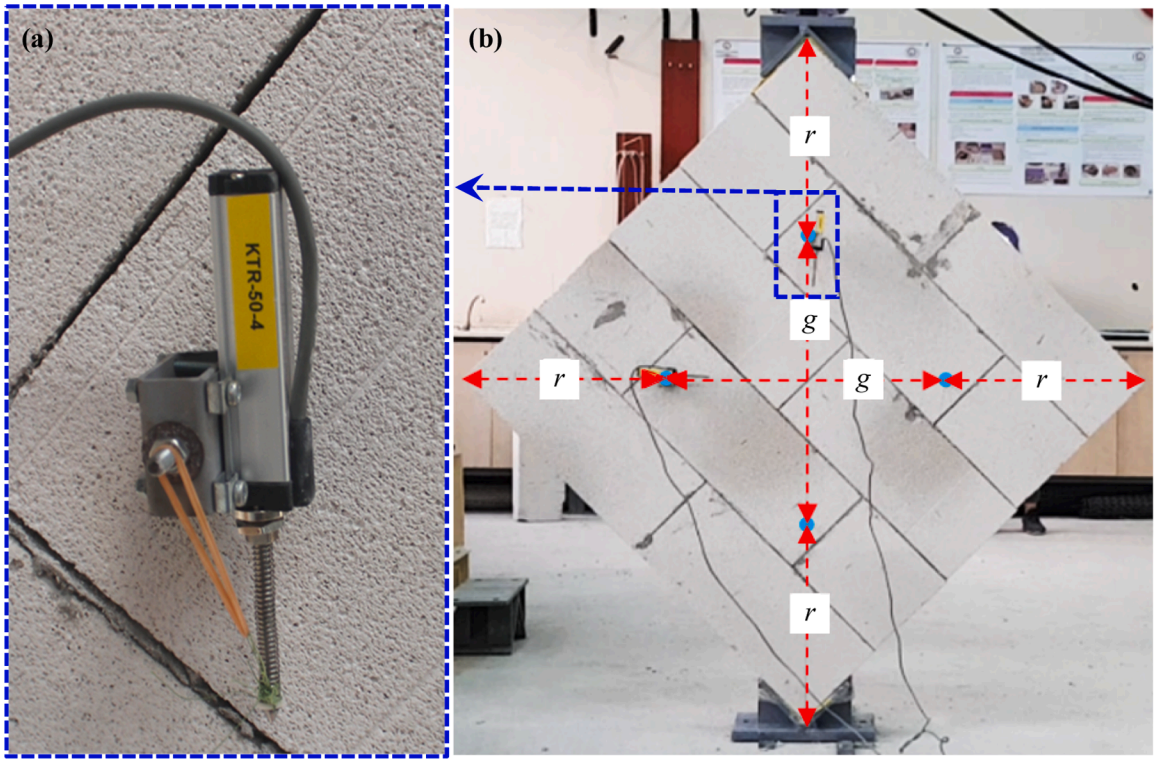


Fig. 4. (a) Placement of LPDTs; (b) Placement distances of LPDTs on the specimen.

including triplet shear tests and diagonal compression tests. The findings of the study demonstrate that both block density and mortar characteristics significantly affect the initial shear strength and failure mode, with lower density blocks and AA-TLM mortars showing reduced performance. Surface preparation, particularly the cleaning of dust after cutting, was also found to notably influence mortar adhesion and, consequently, shear resistance.

The grout used between the AAC units was applied at a thickness of 3 mm, which is common in practice, and the alignment of the specimens was checked with a spirit level. Specimens were prepared without grout and in a staggered manner so that the vertical joints between the AAC units would not overlap the joints in the upper and lower rows. The AAC units arranged in the upper row were placed thoroughly with the help of a mallet (Fig. 2a-e).

3. Material properties

3.1. AAC grout

"Block Bond" type special cement-based grout was used as mortar during the construction of the wall specimens. In order to determine the compressive strength of the grout, 6 specimens of 8 × 16 × 8 cm were prepared. After 28 days of curing, specimens were subjected to uniaxial compression test in accordance with the ASTM C1019 standard [56]. The compressive strengths obtained from AAC grout units are 16.07, 14.24, 15.89, 14.20, 17.26, and 17.59 MPa, respectively, and the mean compressive strength is 15.88 MPa.

Table 2
Calculation parameters for wall specimens.

Average porosity of AAC (n)	Thickness (t) (mm)	Width/Height (w/h) (mm)	Gage length (y/g) (mm)	A_n $[(w+h)/2 \times t \times n]$ (mm^2)	Measured value on spaceman		
					w/h (mm)	y/g (mm)	A_n (mm^2)
80 %	200	250	104/145	40000	252	100/156	40320
		400	167/232	64000	-	-	-
		500	208/290	80000	502	210/290	80320
		600	250/349	96000	-	-	-
		750	313/436	120000	753	310/445	120480
		1000	417/581	160000	1004	420/580	160640
		1200	500/697	192000	1205	500/704	192800
		1400	583/813	224000	-	-	-

3.2. AAC properties

Autoclaved AAC blocks with dimensions of 25 × 60 × 20 cm and class G2 (dry unit volume weight; 350 kg/m^3, compressive strength; 22 kgf/cm^2, thermal conductivity; 0.084 W/mK), which are widely preferred in buildings, were used in the preparation of wall specimens. In order to measure the compressive strength, a total of 8 AAC units, 10 × 10 × 10 cm dimensioned 4 AAC cubes and 10 × 20 × 10 cm dimensioned 4 AAC prisms, were subjected to uniaxial compression test. As a result of the experiments, the mean compressive strength of the cube units was obtained 1.86 MPa and the mean compressive strength of the prism units was obtained 1.73 MPa. In other words, prism units have approximately 8 % lower strength than cube units. The compressive strength values obtained from 10 × 10 × 10 cm cube units are presented in Table 1. Several equations have been reported in the literature that correlate the elastic modulus to density (ρ) and/or compressive strength measured on cubes or prisms for autoclaved aerated concrete (AAC) units [57,58]. According to the CEB Manual [59], the mean modulus of elasticity for AAC units was determined as 955 MPa.

4. Experiments

4.1. Experimental setup

The experimental setup consists of a steel frame with a capacity of 80 tons, a hydraulic piston with a capacity of 50 tons, a load cell with a capacity of 50 tons, displacement reading devices with a capacity of 30 and 50 mm, and two steel loading shoes (Fig. 3).

The wall specimens are placed between two rigid loading shoes, fixed at the bottom and movable at the top (Fig. 3). The piston on the apparatus moves in vertical direction. The load was applied at a rate of 0.5 mm/min under displacement control. Before each experiment, it was ensured that there was no gap between the shoe and the wall and that the shoe was fully fitted to the wall surface. The displacements caused by the piston applying load on the wall specimen are digitally measured with the help of LPDTs placed on the specimen.

4.2. Placement of displacement transducers

Wall specimens subjected to diagonal compression tests are expected to shorten in the direction of force application and lengthen in the direction perpendicular to the loading. Two types of Linear Potentiometer Displacement Transducers (LPDT) of 30 and 50 mm were used to measure these changes (Fig. 4a). LPDTs with a capacity of 30 mm were used in the 25 × 25 cm specimen experiments and LPDTs with a capacity of 50 mm were used in the other specimen experiments. The LPDTs were fixed on the specimens, one in the direction of force application and the other perpendicular to the loading, so as not to restrict the measurement (Fig. 4b).

4.3. Loading shoes

The ASTM E519 [28] test procedure states that the shoe edges should be 1/8 of the length of one edge of the wall specimen. In this study, a total of 10 loading shoe assemblies were prepared, one pair for each specimen test, with a “V” shape and arm lengths of 31.25, 62.50, 93.75, 125, and 150 mm, respectively, in order to comply with the limitation on the loading shoe dimensions specified in the standard. As can be seen in Fig. 3, the prepared metal parts sit in the center of the existing shoe and make the contact surface of the load applied during the test conform to the standard.

4.4. Shear stress-strain calculation method

In this study, the shear stresses and strains of the specimens were determined according to the test procedure specified in the ASTM E519 [28] standard. The corresponding expressions used for shear stress (τ) calculations are given below:

$$\tau = \frac{0.707\,P}{A_n} \tag{1}$$

$$A_n = \left[\frac{(w+h)\,t}{2}\right] n \tag{2}$$

where P, the applied force; A_n, the net area of the wall panel; w, h, and t are the width, height and thickness of the wall panel, respectively. Also, n is percent of the gross area of the unit that is solid and expressed as a decimal. The shear strain (γ) and shear modulus (G) of the wall specimen are calculated by Eqs. (3,4).

$$\gamma = \frac{\Delta x + \Delta y}{g} \tag{3}$$

$$G = \frac{\tau}{\gamma} \tag{4}$$

where Δy, the horizontal elongation; Δx, the vertical shortening; g, the length of the measurement in the direction parallel to the loading shown in Fig. 4. In addition, Table 2 presents the calculation parameters required for the numerical models and the corresponding values measured on experimental specimens.

5. Numerical study

The experimental specimens were also modeled numerically, thereby enabling an examination of the compatibility of the results with theoretical studies. Moreover, the results obtained for a few untested intermediate and oversized cases that have been the focus of previous studies were also considered. Numerical results are compared to those obtained from the corresponding experiments.

Two distinct modelling strategies are available for the analysis of masonry walls, namely macro and micro, depending on the size of

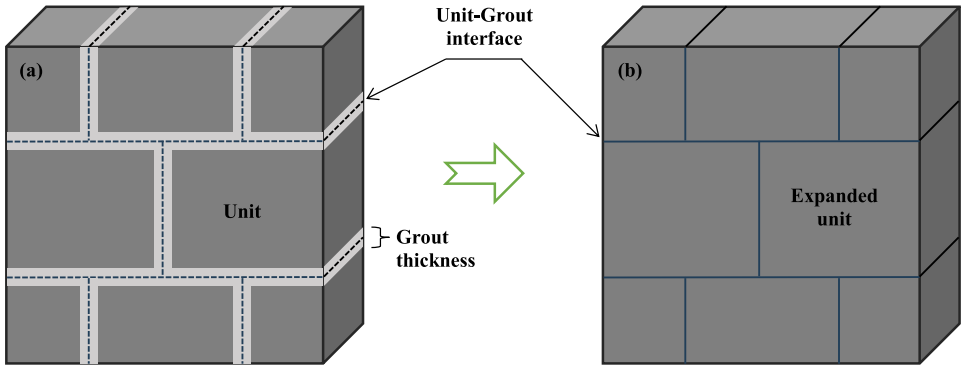


Fig. 5. Finite element modelling approaches: (a) detailed micro-model; (b) simplified micro-model.

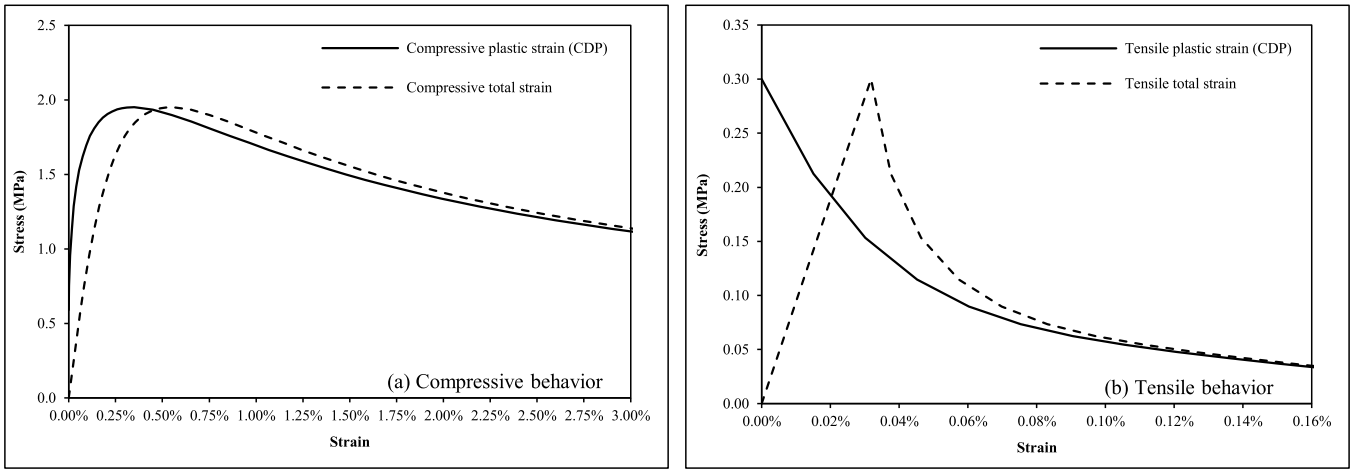


Fig. 6. (a) compressive [77]; (b) tensile [71] behavior of AAC units.

structure. Lourenço [60] provides a comprehensive evaluation of these strategies in his study. In the macro-modelling method, brick-and-mortar units are modelled as a single homogeneous whole. This method is employed in the case of relatively larger and more complex masonry structures. In the micro-modelling method, the brick-and-mortar components are modelled separately. This method can be performed in two ways: the detailed or simplified micro-modelling technique. In the detailed micro-modelling method, brick-and-mortar units are considered discrete finite elements [61,62]. The actual dimensions and material properties are defined separately for both units. This modelling approach necessitates greater computational capacity and time than other methods. In the simplified micro-modelling method, brick units are modelled as finite elements, while non-dimensional cohesive interfacial elements are used to represent the mortar (called as grout in this study) unit [63–68]. Consequently, the grout thickness is neglected, and the brick units are expanded to match the wall dimensions [69]. The interfaces are defined to exhibit both tensile and shear behavior (Fig. 5).

5.1. Concrete damage plasticity (CDP) material model

The Concrete Damaged Plasticity (CDP), an advanced material model derived from the Drucker-Prager model, is used to simulate the inelastic behavior of brittle materials such as concrete and AAC units [70,71]. In the CDP model, the tension meridians of the failure surface are scaled K_m coefficient, while the linear meridians are transformed into parabolic curves via the eccentricity (e) parameter. Dilation angle (β) is expressed as the angle of the failure surface to the hydrostatic axis, and f_{b0}/f_{c0} is the ratio of the biaxial compressive strength of the concrete to the uniaxial compressive strength. For these parameters β, e, f_{b0}/f_{c0}, and K_m, the values 40°, 0.1, 1.16 and 0.667 respectively — recommended in the literature [72–75] and the ABAQUS User Manual [76] — were adopted. The compressive and tensile stress-strain behavior of equivalent AAC specimens was modeled using the constitutive relations proposed by Lee and Fenves [71], and Carreira and Chu [77]. In order to generate CDP input data, a software tool developed by Elkady [78] was utilized (Fig. 6).

5.2. Equivalent material properties for expanded units

Using the simplified micro-modelling technique, an equivalent material was defined for expanded units by treating AAC and grout together. For this purpose, the modulus of elasticity of the grout (E_m) and an expanded unit (E_a), in addition to that of AAC units (E_u), was obtained by Eqs. (5,6) [60,79,80]:

$$E_m = K_e \ f_{cm} \tag{5}$$

$$E_a = \frac{H \ E_u \ E_m}{n \ h_u \ E_m + (n-1) \ h_m \ E_u} \tag{6}$$

where f_{cm}, compressive strength of the grout; K_e, conversion coefficient for modulus of elasticity, which is recommended as 1000 in Eurocode-6 [79]; H, wall height; h_u, brick height; h_m, grout thickness; and n, number of aerated concrete units used along the wall height. In addition, the compressive strength of expanded units was determined as follows:

$$f_{ca} = K_a f_{cu}^{0.7} f_{cm}^{0.3} \tag{7}$$

Table 3
Material properties of AAC units, grout, and expanded units for each specimen.

AAC units			Grout				Expanded units		
f_{cu} (MPa)	E_u (MPa)	G_u (MPa)	h_m (mm)	f_{cm} (MPa)	E_m (MPa)	G_m (MPa)	f_{ca} (MPa)	f_{ta} (MPa)	E_a (MPa)
1.86	955	398	3	15.88	15880	6617	1.95	0.3	954

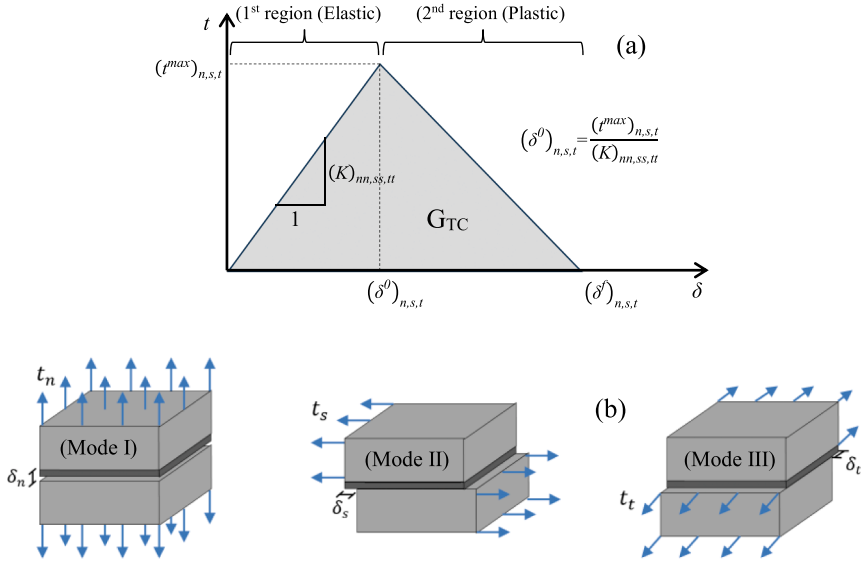


Fig. 7. (a) traction-separation response; (b) failure modes of the joints: (I) tensile cracking; (II-III) shear sliding.

in which K_a was expressed 0.55 according to Eurocode-6 (Table 3.3, AAC, Group 1) [79]. In cases where experimental data are not available, the tensile strength (f_{ta}) of the expanded unit can be considered as 10 % of the compressive strength [81]. In instances where the grout strength is higher than the brick strength, this ratio may be slightly increased. Moreover, the flexural tensile strength (f_{xk2}) that can be used to obtain f_{ta} is presented as a table in Eurocode-6 (Thin layer grout, f_{xk2} = 0.3 MPa) [79]. In this study, it was noticed that these two approaches gave close results. The Poisson ratio of the equivalent unit (γ_a) was considered to be 0.2 as for AAC units and grout. Table 3 presents the calculated material properties that were utilized in the modelling for AAC units, grout, and expanded units. The relationship between the modulus of elasticity and rigidity is defined by $E = 2\,G(1+\gamma)$. The expressions G_u and G_m represent the rigidity modules of the AAC units and grout, respectively.

In cyclic loading cases, the damage parameters dc (compressive), and dt (tensile) cause a decrease in compressive and tensile strengths. In the absence of these definitions within the analysis, the behavior under monotonic pushover load can be achieved [13,14].

5.3. Surface-based cohesive behavior

Materials such as grout, which bond masonry units like bricks and AAC blocks, have a significant influence on the overall wall strength and damage evolution. In this study, the grout placed between AAC units was modeled using a surface-based cohesive approach based on the Cohesive Zone Model (CZM). This modeling technique is designed to capture interfacial damage evolution by accounting for both the unit material and interface properties. The joint behavior before and after damage is described using a bilinear traction–separation law, which reflects failure mechanisms in three directions: normal, in-plane shear, and out-of-plane shear. For simplification purposes in this study, the in-plane and out-of-plane shear responses were considered equivalent. Additionally, the implementation of "hard contact" assumes that normal stresses are fully transmitted across interfaces, without permitting penetration between contact surfaces.

The interface properties utilized in the Cohesive Zone Model (CZM) approach do not represent physical materials, but rather idealized, zero-thickness interfaces between adjacent finite element units. In this modeling technique, the traction–separation behavior is typically characterized by two distinct regions (Fig. 7a). The first region extends from the origin to the point of damage initiation, representing the initial stiffness of the cohesive link. Within this region, the material response is linear-elastic, and no degradation occurs until the peak traction is reached. At the end of the region, the t_n^{max} (normal) and t_s^{max}, t_t^{max} (shear) stresses that define the onset of damage are accessed. The second region corresponds to the phase between damage initiation and complete separation, during which stiffness degradation and progressive damage occur. As the relative displacements increase beyond the peak traction point, the initial elastic response (traction) is gradually replaced by interface separation. This damage evolution is governed by three distinct failure modes. As illustrated in Fig. 7b, Mode I corresponds to failure in the normal direction, while Modes II and III represent in-plane and out-of-plane shear failures, respectively, both associated with crack propagation. In this study, it is assumed that the mechanical properties of the wall joints are identical in both shear directions.

The stresses in the elastic region of the tensile-separation behavior are expressed as a vector (t) as given in Eqs. (8–10). The displacement vector (δ) at the contact interface is defined depending on the elastic stiffness matrix (K). This matrix represents the linear behavior before the joints are damaged. The vector t is composed of stress components in three directions (t_n, t_s, t_t) and the vector δ is composed of displacement (separation) components (δ_n, δ_s, δ_t) as follows:

$$[t] = \begin{bmatrix} t_n \\ t_s \\ t_t \end{bmatrix} = \begin{bmatrix} K_{nn} & 0 & 0 \\ 0 & K_{ss} & 0 \\ 0 & 0 & K_{tt} \end{bmatrix} \begin{bmatrix} \delta_n \\ \delta_s \\ \delta_t \end{bmatrix} = [K][\delta] \tag{8}$$

Table 4
Linear and nonlinear contact properties between extended AAC units.

Traction–separation behavior (Stiffness) (N/mm^3) [60]		Friction coefficient [13,14]	Damage initiation (Interface strength) (MPa) [79]		Damage evolution (Critical fracture energy) (N/m)	
K_{nn}	K_{ss}=K_{tt}	μ	t_n^{max}	t_s^{max}=t_t^{max}	G_{IC}	G_{IIC}=G_{IIIC}
338.6	141.1	0.62	0.065	0.084	2.25	6.75

$$K_{nn} = \frac{E_u \ E_m}{h_m(E_u - E_m)} \tag{9}$$

$$K_{ss} = K_{tt} = \frac{G_u \ G_m}{h_m(G_u - G_m)} \tag{10}$$

According to the simplified micro modelling approach, the stiffness of the interface is expressed depending on the properties of the joints (stiffness and thickness). In Eqs. (9,10), stiffness in the normal direction of the surface is given as K_{nn} and stiffnesses in the shear directions are given as K_{ss} and K_{tt} [60,63,80]. The contact parameters used in the simplified micro modelling of the specimens are presented in Table 4.

The quadratic stress criterion was used to determine the damage behavior [80]. This criterion was adopted to effectively identify the damage initiation of joints subjected to mixed mode loading such as masonry walls [82]. Furthermore, the coefficient of friction of the masonry joints has been defined with the objective of simulating the post-failure shear tangential behavior. Critical sliding shear stress is obtained based on the friction law ($\sigma_{sliding} = \mu \ \sigma_n$), which is subject to a linear relationship between the coefficient of friction and normal compressive stress [83]. Where μ, friction coefficient of interface between the masonry joints; σ_n, normal contact pressure stress in masonry joint interfaces.

In order to determine the strength of the interface connection and critical fracture energy, it is necessary to perform some additional experiments under tensile and shear effects [13,83–85]. The grout and AAC units used in this study are similar to those of Bikçe, et al. [13]. However, in cases where the grout strength exceeds that of the brick units, the separation surface may occur within the brick rather than

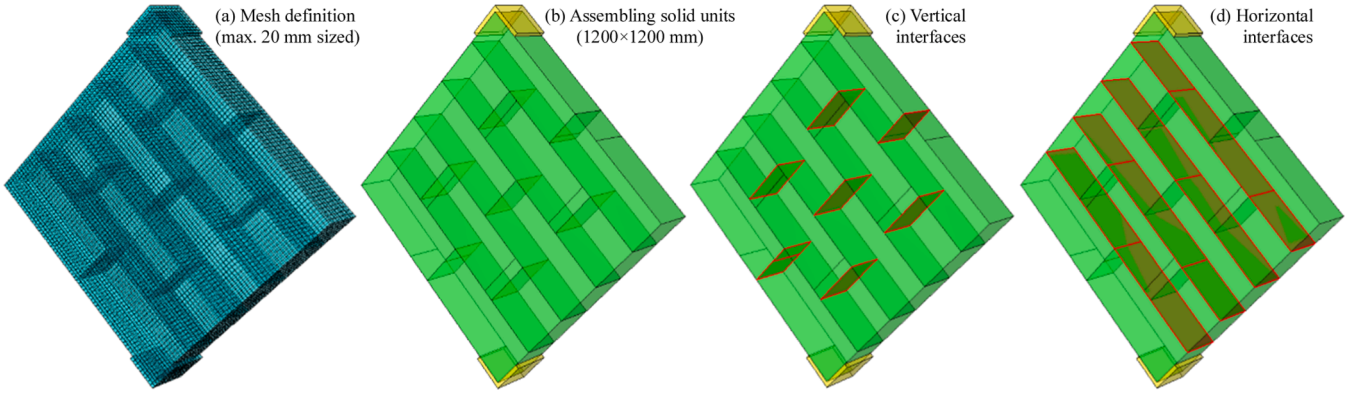


Fig. 8. Simplified micro model illustrations of 120 × 120 cm specimen.

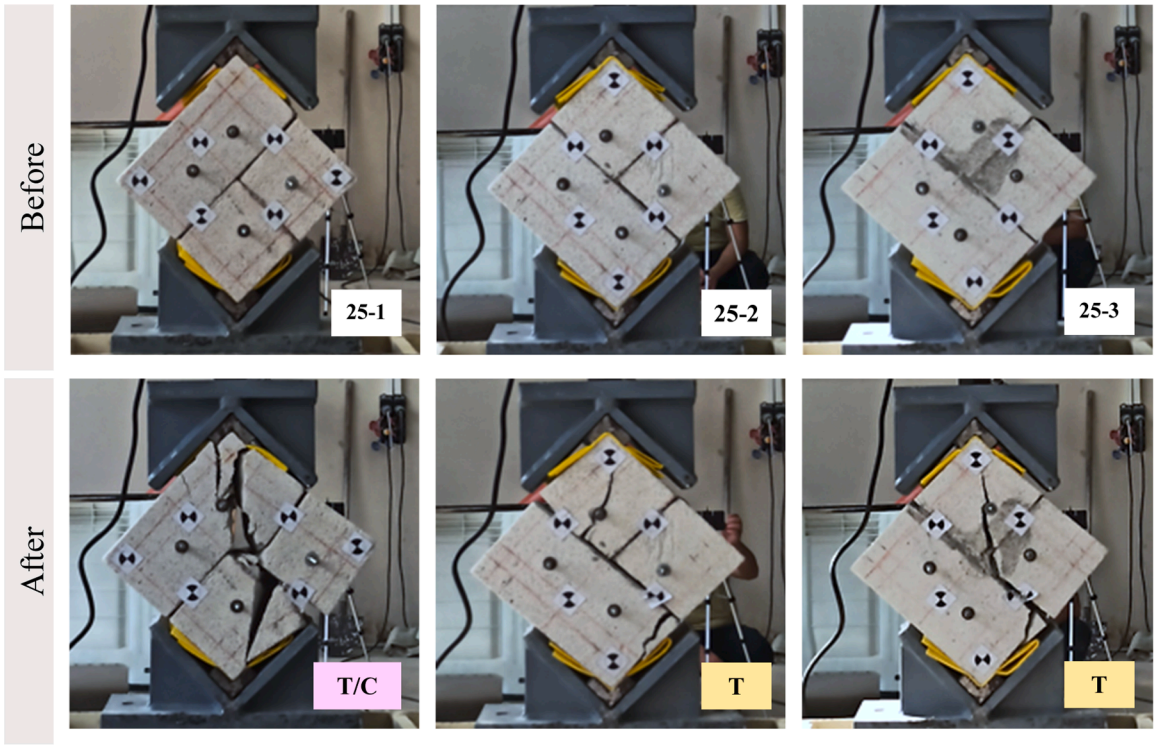


Fig. 9. Images of 25 × 25 cm wall specimens before and after loading.

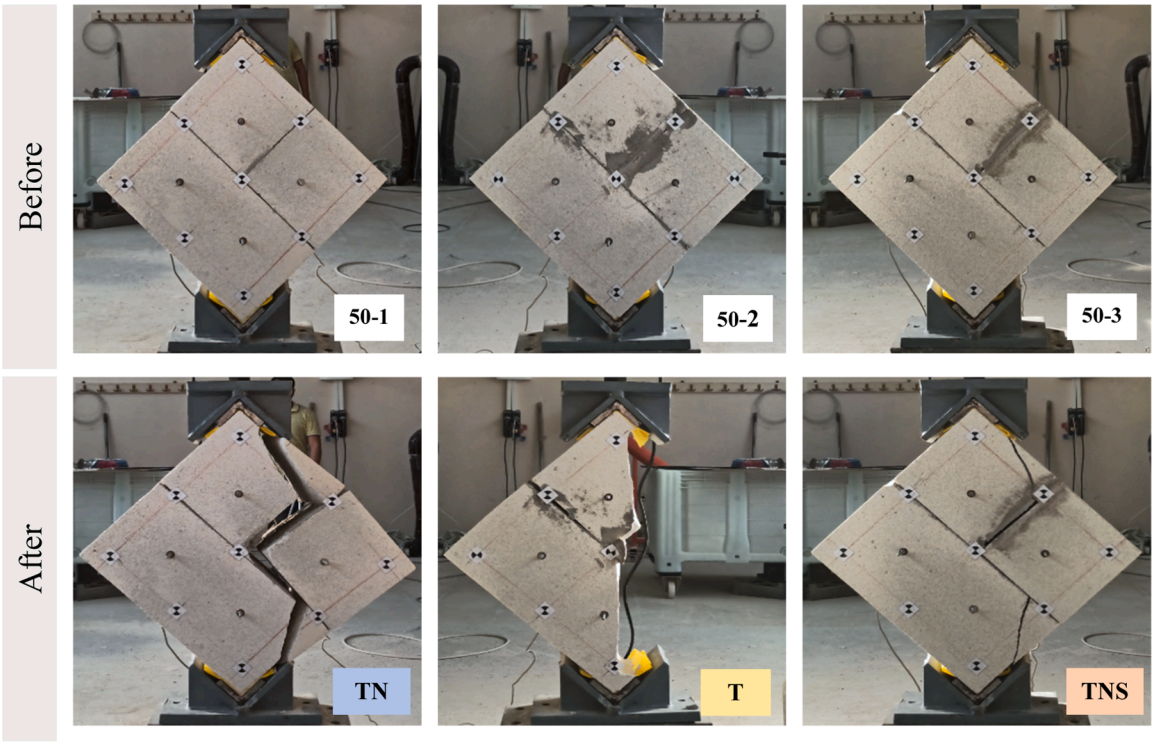


Fig. 10. Images of 50 × 50 cm wall specimens before and after loading.

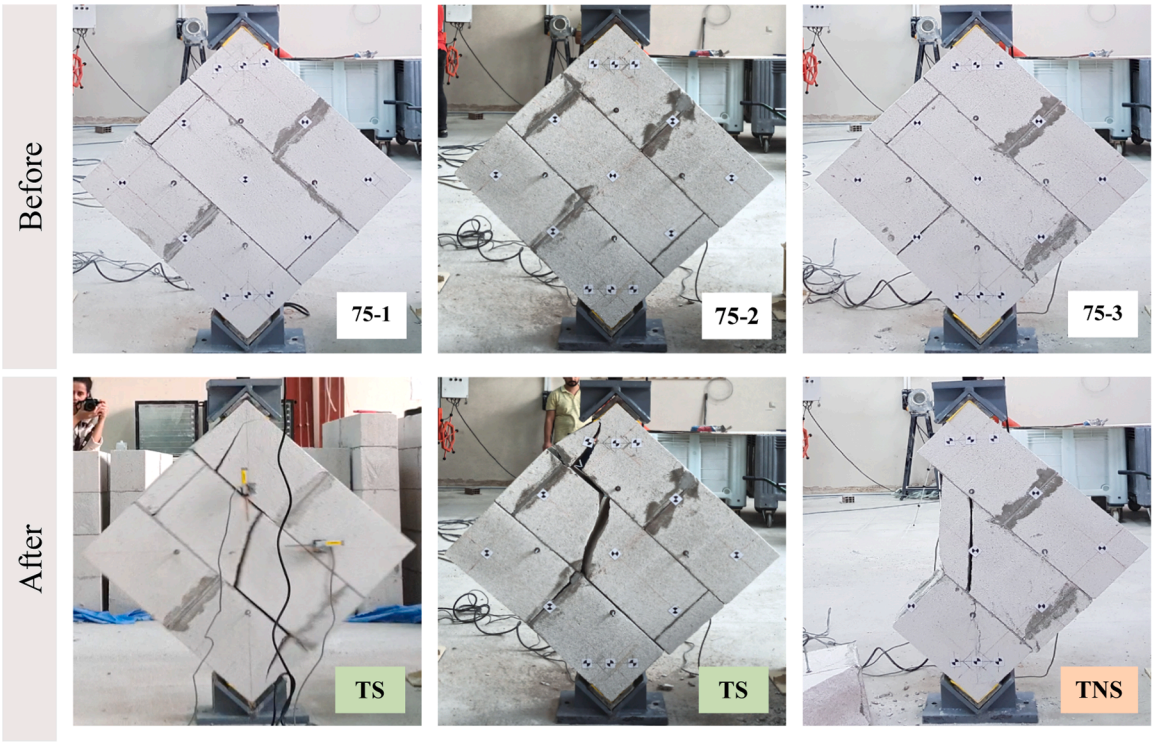


Fig. 11. Images of 75 × 75 cm wall specimens before and after loading.

within the grout [34,86]. For this purpose, Eurocode 6 includes additional conditions that the interface strengths cannot exceed the limits determined according to the compressive strength (f_b) of the joined unit elements to a certain extent. Accordingly, the upper limit strength values determined for the interface to be used in the analytical model were calculated by Eqs. (11,12) and presented in Table 4 (defined f_{xk1} for tension and f_{vk} for shear in Eurocode 6).

$$t_n^{max} = 0.035\, f_{cu} \tag{11}$$

$$(t^{max})_{s,t} = 0.045\, f_{cu} \tag{12}$$

Once the conditions for damage initiation are reached, the stiffness

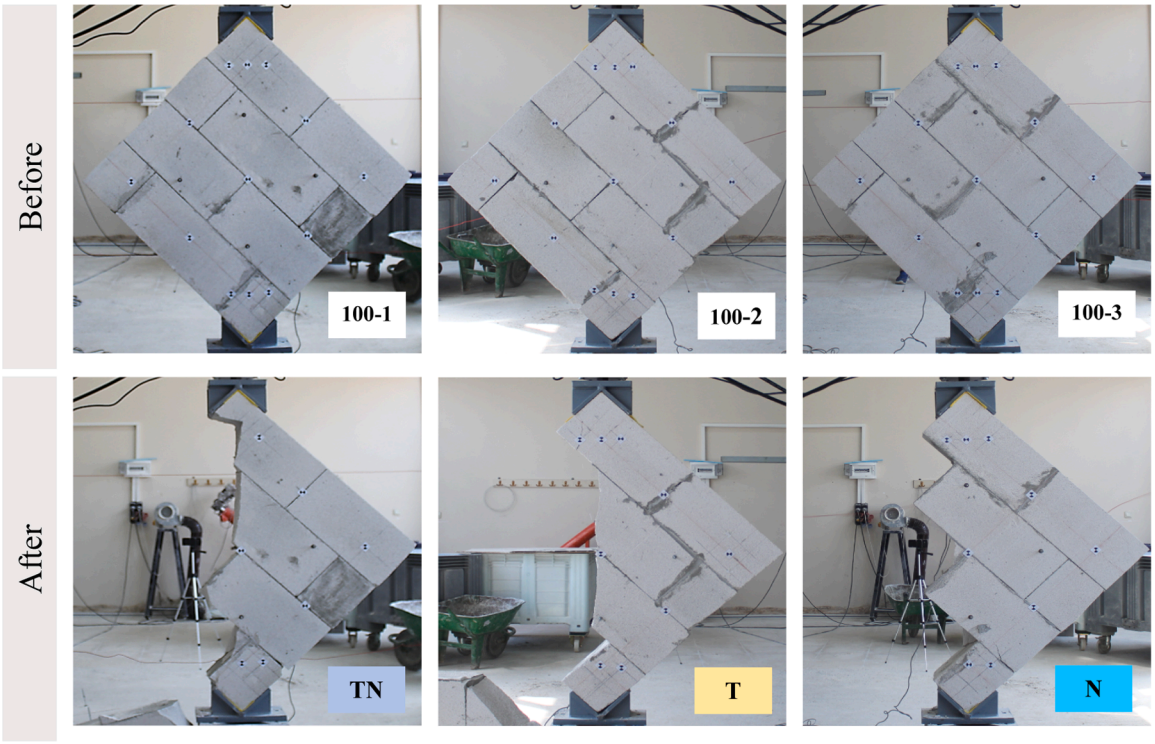


Fig. 12. Images of 100 × 100 cm wall specimens before and after loading.

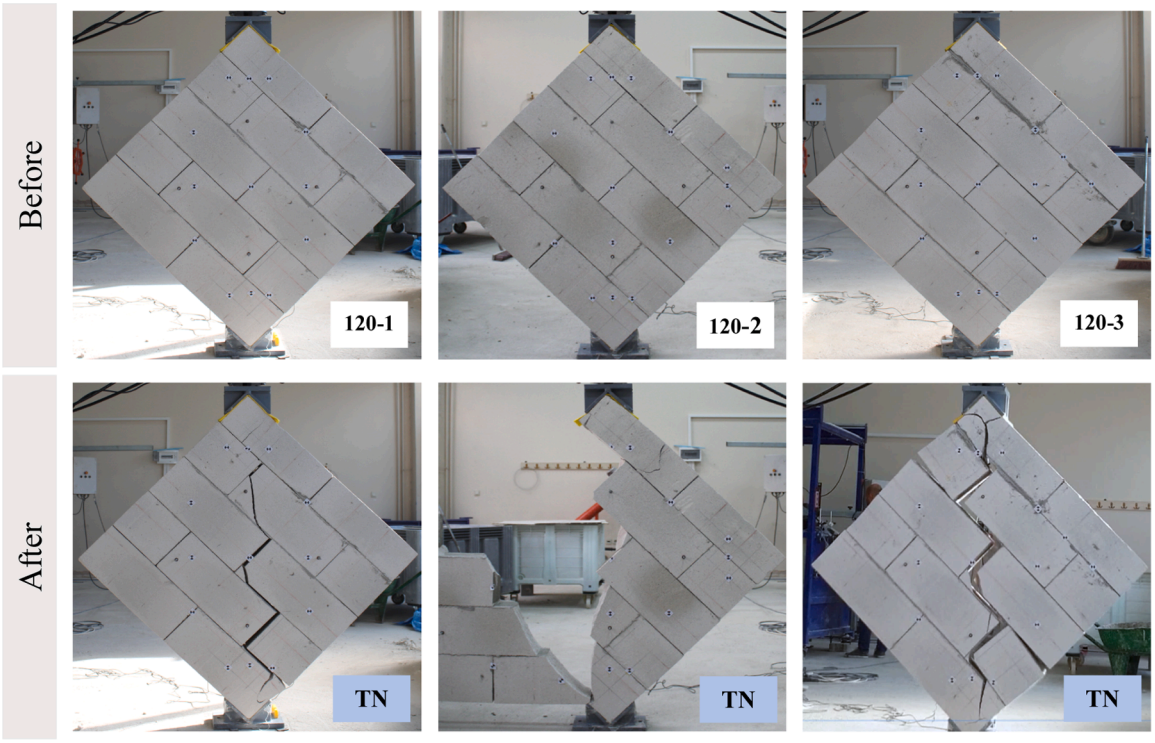


Fig. 13. Images of 120 × 120 cm wall specimens before and after loading.

degradation begins due to the existence of brittle cracks. To determine the damage evolution of experimental behavior, the critical mixed-mode fracture energy (G_{TC}) is obtained using the Benzeggagh-Kenane (BK) law [80,87,88] according to Eq. (13):

$$G_{TC} = G_{IC} + (G_{IIC} - G_{IC})\left[\frac{G_{shear}}{G_I + G_{shear}}\right]^{\eta} \tag{13}$$

The G_I and G_{shear} values represent the energy release rates for Mode I and Mode II-III, respectively, and can be calculated from the nodal forces and displacements obtained from the solution of the finite element

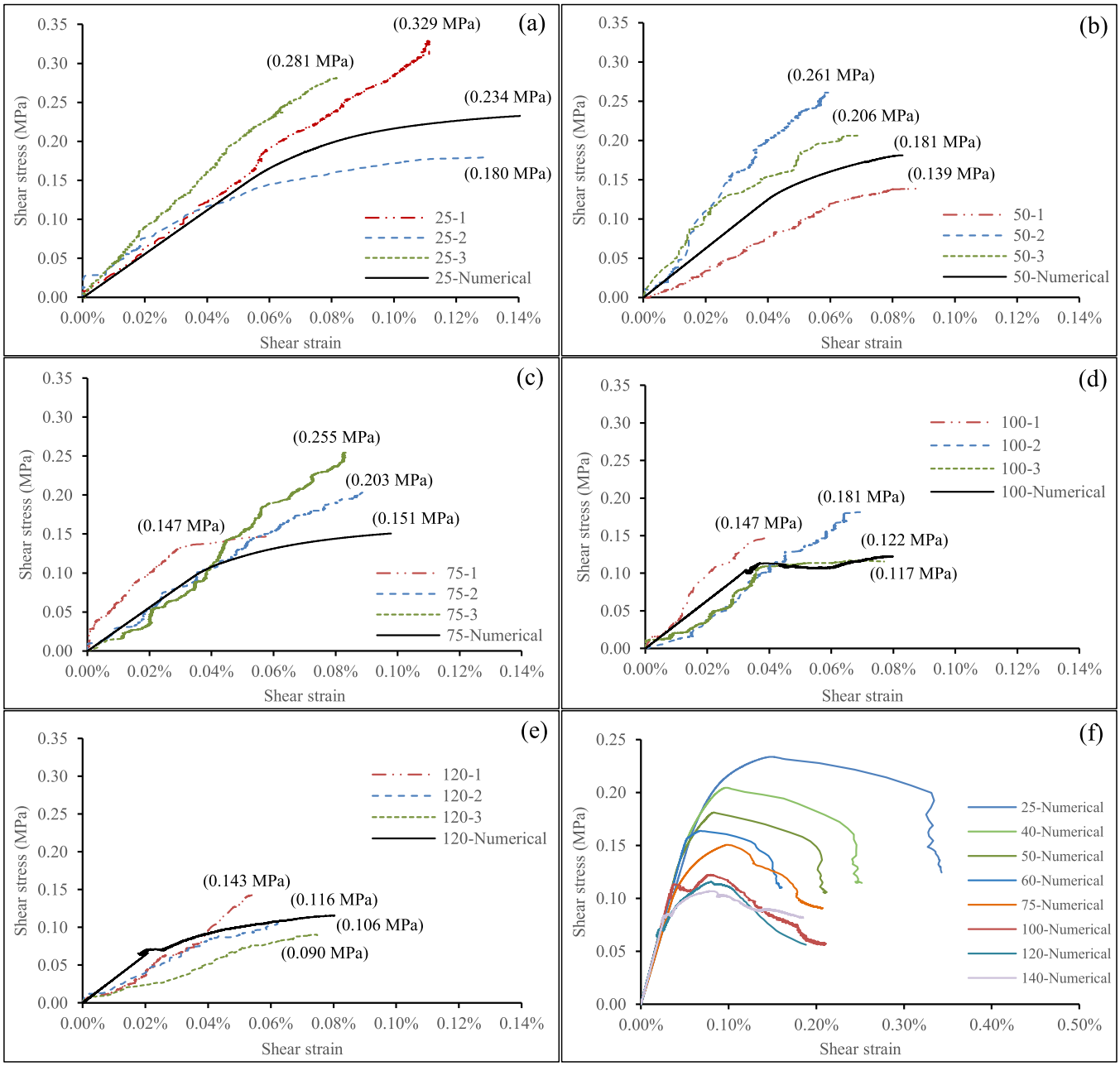


Fig. 14. Comparison of shear stress-strain curves of the specimens in the same group.

model [88]. In Eq. (13), the normal (G_{IC}) and shear ($G_{IIC} = G_{IIIC}$) fracture energies were determined by calibration to be most consistent with the experimental results and are presented in Table 4. These considered energy values were seen to be consistent with experimental brittle fracture cases involving AAC specimens [89]. Additionally, the BK material parameter (η) controls the shape of the mixed-mode fracture envelope. To the authors' knowledge, no prior experimental studies have evaluated η for AAC units or their typical grout types. Based on the BK law, η was set to 1.75, reflecting the brittle behavior of masonry joints and lightweight AAC units, as well as the commonly used range of 1.5–2.0 for such materials [88,90].

5.4. Finite element modelling and analysis

In this study, three-dimensional finite element models (FEM) were developed to simulate the behavior of the experimental specimens (Fig. 8a-d) [76]. A non-linear explicit dynamic solution method was employed to perform numerical analyses. This approach was selected to mitigate potential numerical instabilities and convergence issues arising from brittle damage and abrupt stiffness degradation inherent in nonlinear modeling.

The simplified micro modeling technique was employed to simulate the behavior of the experimental specimens. For this purpose, the mechanical behavior and material properties of each constituent component of the wall specimens—namely, AAC units, grout, and loading shoes—had to be defined. Considering a joint thickness of 3 mm, the AAC units were geometrically expanded and interconnected using a surface-based cohesive modeling approach. The steel loading shoes were modeled as linear elastic, and modulus of elasticity was considered as $E_s = 2 \times 10^5$ MPa. The numerical models were generated using C3D8R solid elements (8-node brick elements with reduced integration). Based on the scale enlargement, the mesh size for the AAC units was assigned as follows: 5 mm for 25 mm blocks, 10 mm for 40, 50 mm, 15 mm for 60, 75 mm, and 20 mm for 100, 120, 140 mm specimens, respectively.

Table 5
Resultant mechanical parameters for experimental specimens.

Size (cm)	Exp. No	Spec. No	Load (P) (kN)			(Δx+Δy) at P_{max} (mm)			Shear strength (S_s) (MPa)				Shear strain at $(S_s)_{max}$ (γ) (mm/mm)			Shear modulus (G) (MPa)
			Max	Mean		Max	Mean		Max	Mean	SD	CV	Max	Mean		
25 × 25	1	25–1	18.60	14.90		0.174	0.168		0.329	0.263	0.0621	23.6 %	0.111 %	0.108 %		295.5
	2	25–2	10.17			0.203			0.180				0.130 %			138.0
	3	25–3	15.91			0.127			0.281				0.082 %			344.8
50 × 50	4	50–1	15.71	22.86		0.259	0.211		0.139	0.202	0.0500	24.7 %	0.089 %	0.073 %		155.6
	5	50–2	29.54			0.172			0.261				0.059 %			440.0
	6	50–3	23.34			0.203			0.206				0.070 %			295.3
75 × 75	7	75–1	24.91	34.20		0.256	0.340		0.147	0.202	0.0440	21.8 %	0.057 %	0.076 %		255.3
	8	75–2	34.50			0.394			0.203				0.089 %			229.3
	9	75–3	43.20			0.370			0.255				0.083 %			306.0
100 × 100	10	100–1	33.17	33.53		0.223	0.335		0.147	0.148	0.0264	17.8 %	0.038 %	0.058 %		381.6
	11	100–2	41.02			0.402			0.181				0.069 %			264.4
	12	100–3	26.40			0.381			0.117				0.066 %			177.6
120 × 120	13	120–1	38.71	30.64		0.380	0.449		0.143	0.113	0.0219	19.4 %	0.054 %	0.064 %		264.2
	14	120–2	28.70			0.440			0.106				0.062 %			169.1
	15	120–3	24.53			0.527			0.090				0.074 %			121.3

In the model, the lower loading shoe is fixed, while the upper shoe is hinged and free to move along the loading direction. The vertical load was applied under displacement control using a constant-velocity ramp, resulting in a linear displacement of 3 mm over a duration of 30 s. In order to calibrate the analytical results with the experimental observations, damage evolution in normal direction of the vertical interfaces was deliberately restricted (Fig. 8d). This restriction was implemented by increasing the initial tensile strength and the critical fracture energy in the normal direction by 10 %. Apart from this modification, all necessary material definitions were comprehensively included for these interfaces. At the horizontal interfaces, all parameters related to elastic and plastic behavior were defined without imposing any further constraints, in order to preserve the stability of the specimens (Fig. 8d).

6. Experimental and numerical results

The experimental specimen groups in 25 × 25, 50 × 50, 75 × 75, 100 × 100, and 120 × 120 cm sizes, which were subjected to diagonal shear tests, are presented in Figs. 9–13. During the tests, the vertical reaction force on the bottom support and displacement values at the reference points defined on the specimens were measured and shear stress-strain relationships are plotted (Fig. 14a-e). The shear strength and strain results obtained from the experiments are also presented in Table 5. In addition to the mean shear strength values, the Standard Deviation (SD), and the Coefficient of Variation (CV) were calculated for each test group and are presented separately in the table.

For comparison and verification purposes, the results obtained from numerical modeling, all details of which are given in previous section, are presented in conjunction with the experimental results (Figs. 15–17). For additional intermediate and larger sized samples of 40 × 40, 60 × 60, and 140 × 140 cm, which were not experimented, numerical analyses were performed with similar steps to provide more information about the specimen size effect (Figs. 18–20). Moreover, Fig. 14f, and Table 6 provide a comparison of the numerical results within each other.

The mean shear strengths (S_s) and the corresponding shear strain (γ) values obtained from the experiments and numerical models according to the specimen sizes are presented in Tables 5,6. When these values are plotted on the same graph, distinct trend lines representing the variation with respect to specimen size are obtained (Fig. 21a,b). The trend lines were presented in logarithmic form, in accordance with Bažant's [91] suggestion concerning the size effect.

FEMA 306 [92] is a standard for classifying damage modes for unreinforced walls. According to this standard, damage can be categorized as joint sliding failure, diagonal tensile failure, and toe crushing failure. Moreover, Lim [41] experimentally classified the damage into five distinct categories: diagonal tension failure, non-diagonal failure, sliding failure, toe-crushing failure, and combined failure (tensile–sliding). In this case, combined failure can be seen in both diagonal and non-diagonal modes.

Upon examination of the fracture patterns exhibited by specimens with equivalent dimensions, a variety of damage types were observed. In this study, specimen damage was categorized and named in accordance with FEMA 306. Sliding failure (S) is a pattern in which cracks happen along the joint surface without involving AAC units. This situation is observed as linear sliding of an adjacent AAC row relative to another along the grout. Two types of diagonal tensile failure (T/N) refer to a failure caused by cracks in the diagonal direction of the specimen in AAC unit and/or grout. The damage evolution is observed as tensile failure in the units (T) and/or separation of the joint mostly in the normal direction (N). Finally, toe crushing failure (C) involves crushing an AAC unit at its pointed end. In general, these failure modes are not observed in their pure form; rather, they are seen as combinations of these modes [41,48]. Some types of combined failure modes seen in experiments were named as follows: tensile–separation (TN), tensile–sliding (TS), separation–sliding (NS), tensile–separation–sliding (TNS), (Figs. 9–13). Toe crushing (C) can also be added to these failure modes.

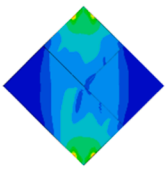
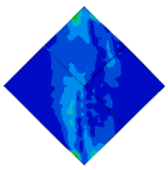
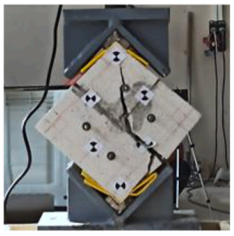
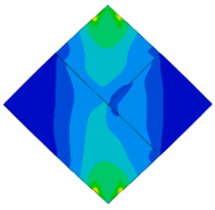
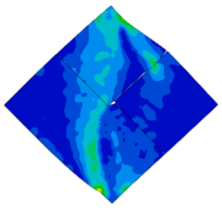
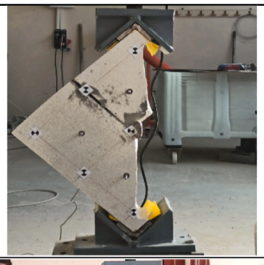
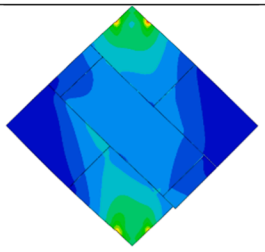
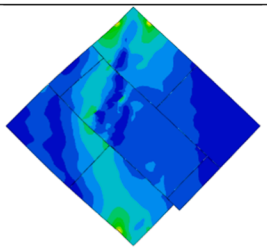
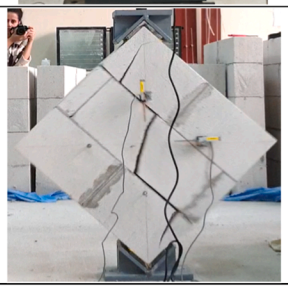
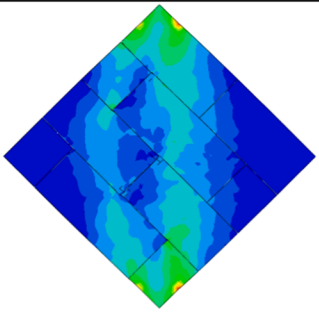
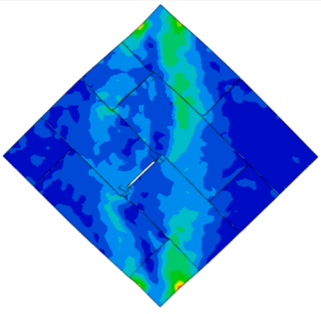
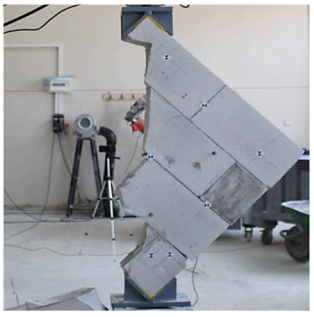
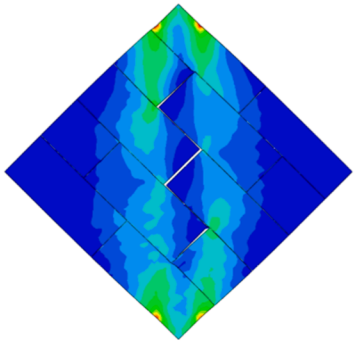
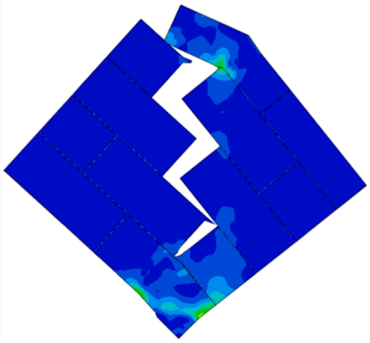
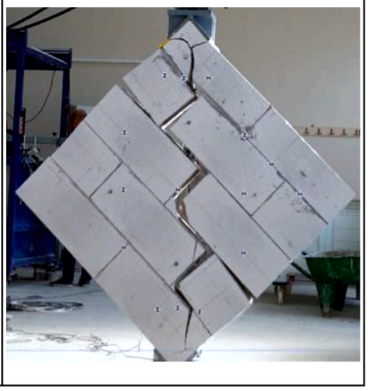
	Von Mises Stress (N/mm^2)	Pre-Failure	Post-Failure	Experimental Cases
25×25 cm	+1.925e+00 +1.766e+00 +1.607e+00 +1.448e+00 +1.289e+00 +1.130e+00 +9.716e-01 +8.127e-01 +6.538e-01 +4.949e-01 +3.360e-01 +1.771e-01 +1.821e-02	 T = 3.25 sn	 T = 3.30 sn	
50×50 cm	+1.635e+00 +1.499e+00 +1.363e+00 +1.226e+00 +1.090e+00 +9.539e-01 +8.177e-01 +6.815e-01 +5.453e-01 +4.091e-01 +2.729e-01 +1.367e-01 +5.471e-04	 T = 4.40 sn	 T = 4.60 sn	
75×75 cm	+1.125e+00 +1.032e+00 +9.381e-01 +8.446e-01 +7.511e-01 +6.576e-01 +5.641e-01 +4.705e-01 +3.770e-01 +2.835e-01 +1.900e-01 +9.645e-02 +2.927e-03	 T = 6.20 sn	 T = 6.40 sn	
100×100 cm	+1.086e+00 +9.962e-01 +9.067e-01 +8.172e-01 +7.277e-01 +6.382e-01 +5.487e-01 +4.592e-01 +3.697e-01 +2.802e-01 +1.907e-01 +1.012e-01 +1.171e-02	 T = 7.50 sn	 T = 8.00 sn	
120×120 cm	+7.432e-01 +6.815e-01 +6.198e-01 +5.581e-01 +4.964e-01 +4.347e-01 +3.730e-01 +3.113e-01 +2.496e-01 +1.879e-01 +1.262e-01 +6.450e-02 +2.803e-03	 T = 11.60 sn	 T = 11.80 sn	

Fig. 15. Von Mises stress distribution (VM).

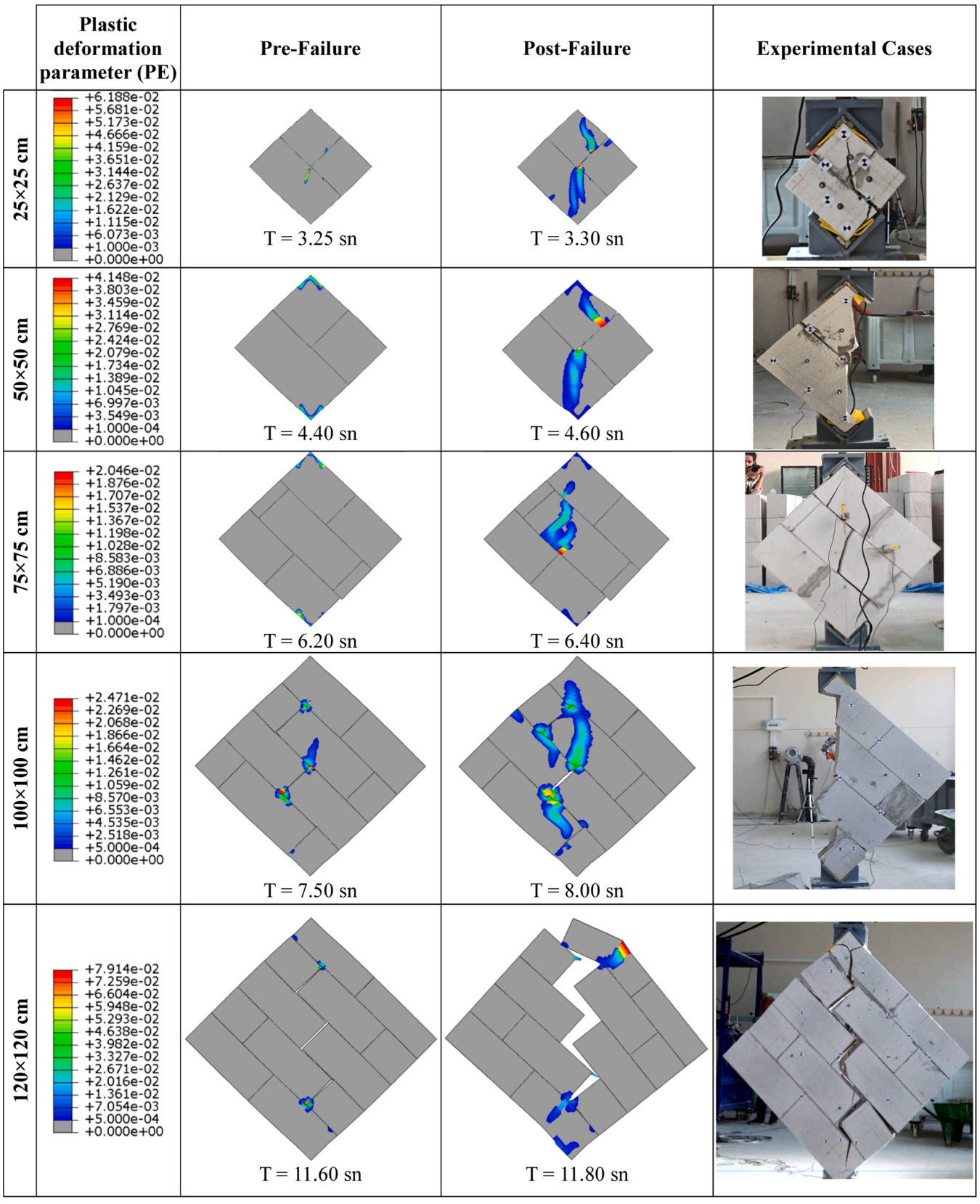


Fig. 16. Plastic deformation parameter (PE).

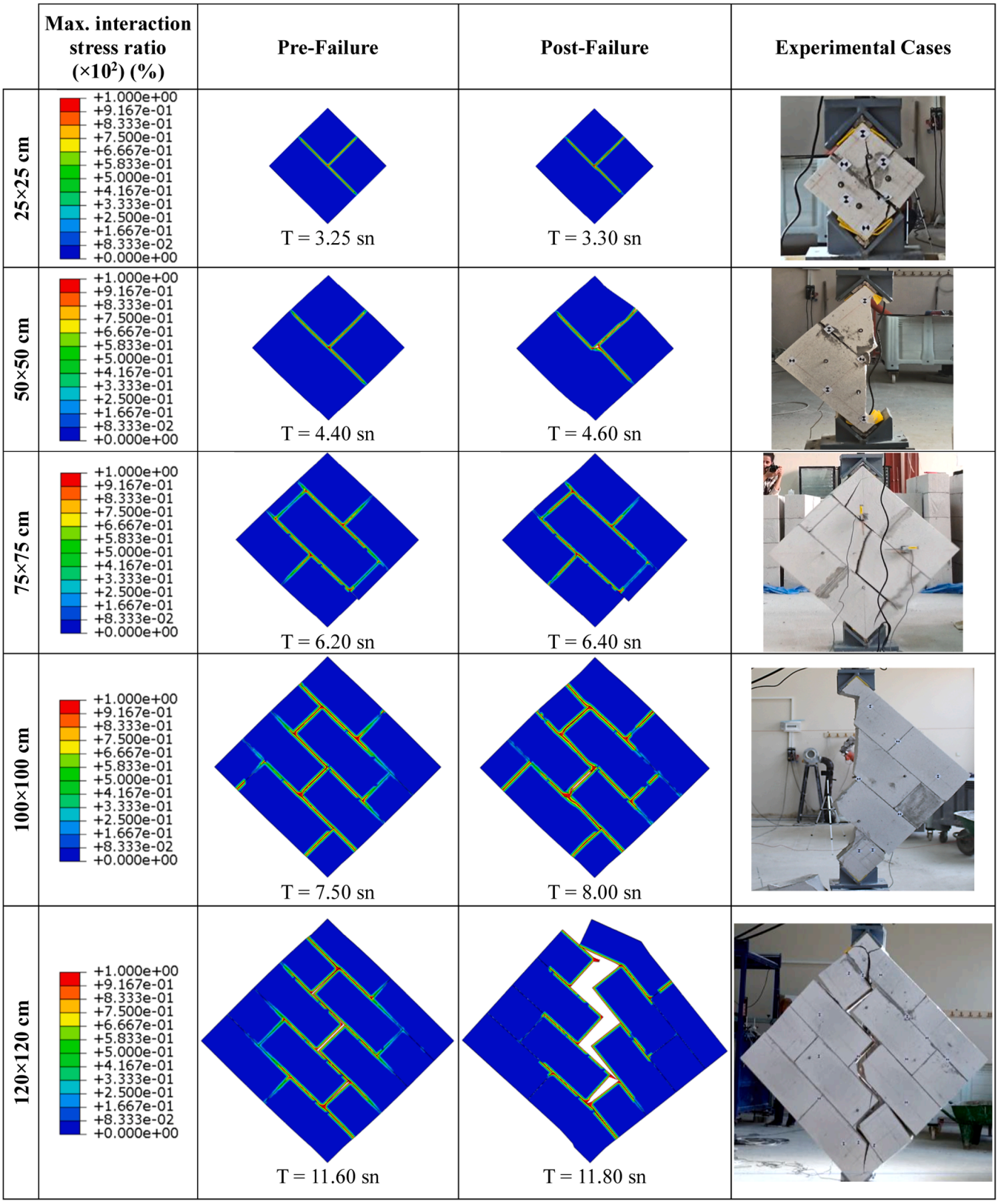


Fig. 17. Maximum interaction stress ratio (CSMAX).

6.1. *Interpretation of results*

Despite the similarity in fracture patterns among the same size groups, the observed discrepancies are presumed to stem from slight variations in the mechanical properties of the grout and AAC, in addition to inconsistencies arising from workmanship [34]. The interface bonding quality between adjacent AAC units is considered to have a more substantial influence on the shear strength and failure modes of small-scale specimens compared to those of larger ones (Figs. 9–13). As a result of this, it is understood that as the specimen size increases, the

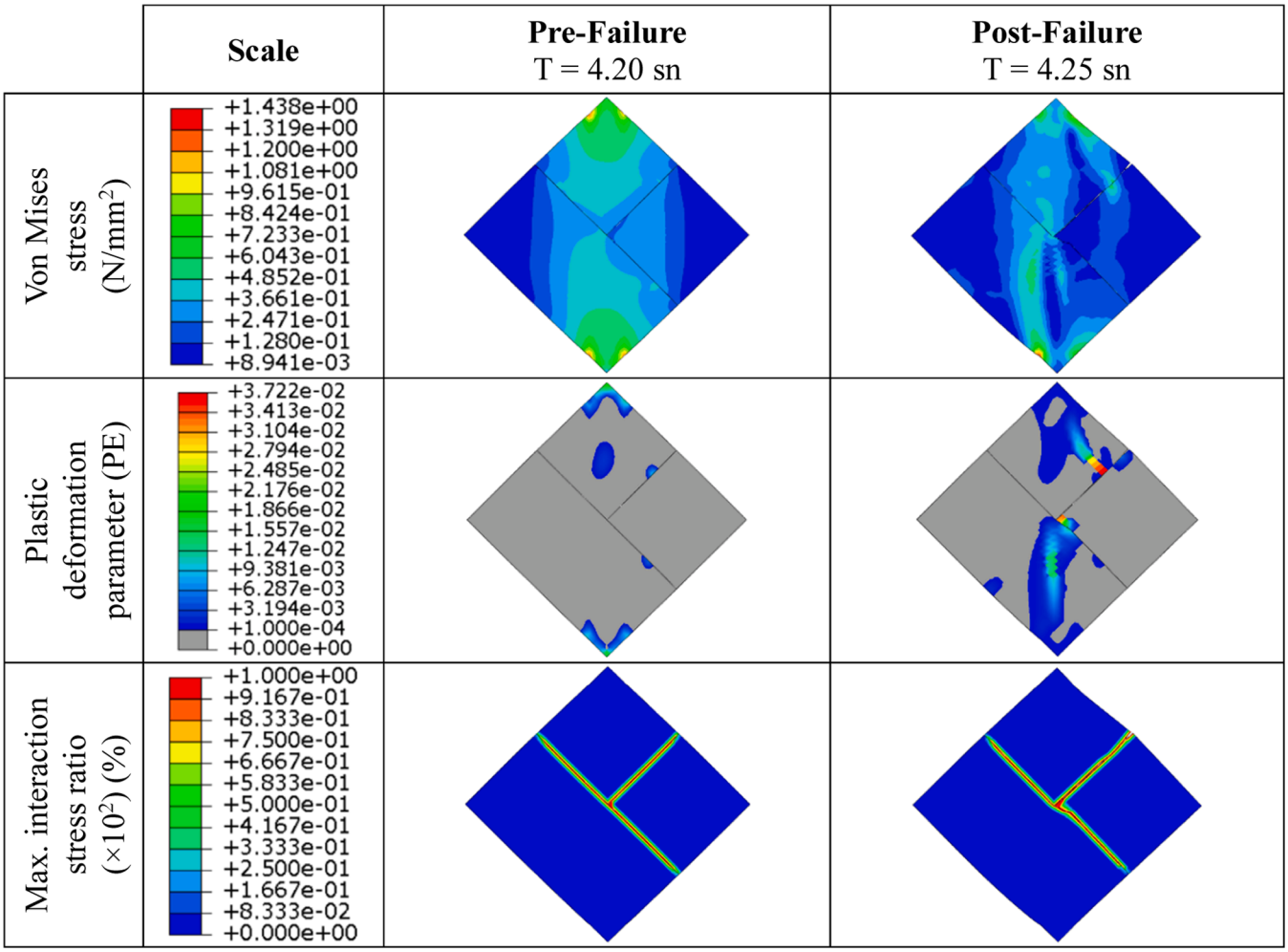


Fig. 18. Findings for the additional size 40 × 40 cm.

variation in strength among specimens of the same size group tends to decrease (Fig. 14a-e, Fig. 21a). This situation can be understood by examining the reduction in the Coefficient of Variation (CV), as presented in Table 5. Moreover, as the specimen size increases, the fracture line tends to adopt a more distinctly diagonal orientation. This behavior can be attributed to the increased uniformity in joint distribution, which arises from a reduction in AAC unit size relative to the overall specimen dimensions. However, higher strength values were obtained in the specimens where diagonal tensile failure (T) was dominant, as opposed to those exhibiting joint separation (N) or sliding (S) failure. In these specimens, failure was observed to be more brittle, accompanied by reduced strain levels (Fig. 14a,b). Conversely, in specimens that experienced joint separation or sliding, the shear stress–strain curves were relatively flat, indicating that shear stress remained nearly constant while strain continued to increase (Fig. 14c,d).

The numerical results exhibit good agreement with the experimental findings, particularly in terms of the stress–strain relationships (Fig. 14a–e). In addition, comparative pre- and post-failure images of the Von Mises stress distribution (VM), plastic deformation parameter (PE), and maximum interaction stress ratio (CSMAX), which provide key insights into fracture behavior, are presented in Figs. 15–20. The plastic deformation patterns observed in the 25 × 25, 50 × 50, and 75 × 75 specimens closely resemble the experimentally obtained fracture modes (Fig. 16). Moreover, the partial sliding (S) behavior detected between joints in the 75 × 75 specimen was also captured in the numerical simulations. In the 100 × 100 and 120 × 120 specimens, the combined tension–separation (TN) failure mode identified experimentally was successfully reproduced in the numerical models. Additionally, the initial slope of the stress–strain curves in the numerical analyses aligns well with those observed in the experimental data (Fig. 14a–e). Examination of both experimental and numerical analyses indicates that small-size specimens primarily exhibit tensile failure or unit sliding, while joint separation emerges as the prevailing fracture mechanism with increasing specimen size. As seen in Fig. 14f, the initial slopes of the numerically obtained stress-strain curves are nearly identical. This similarity is thought to result from the use of identical elastic properties for the AAC units and interfaces in all numerical models, regardless of specimen size. As a result, no significant difference in initial stiffness is observed between specimens of different dimensions. Under test conditions, specimens of the same size may exhibit differences in initial stiffness (Fig. 14a–e). These variations are considered reasonable and are attributed to workmanship effects. It is believed that the results would become more consistent with increasing number of test specimens.

6.2. *Mathematical findings for the specimen size effect*

When Fig. 21 is examined, it is seen that while higher shear strength and corresponding strain are obtained in small sized specimens, these values decrease as the specimen size increases. Based on only the experimental results using AAC wall specimens with a thickness of 20 cm, Eqs. (13,14) are derived to give the logarithmic trend lines as:

$$(\tau_e)_{trd} = -8.8 \times 10^{-2} \ln(D) + 0.7527 \quad (13)$$

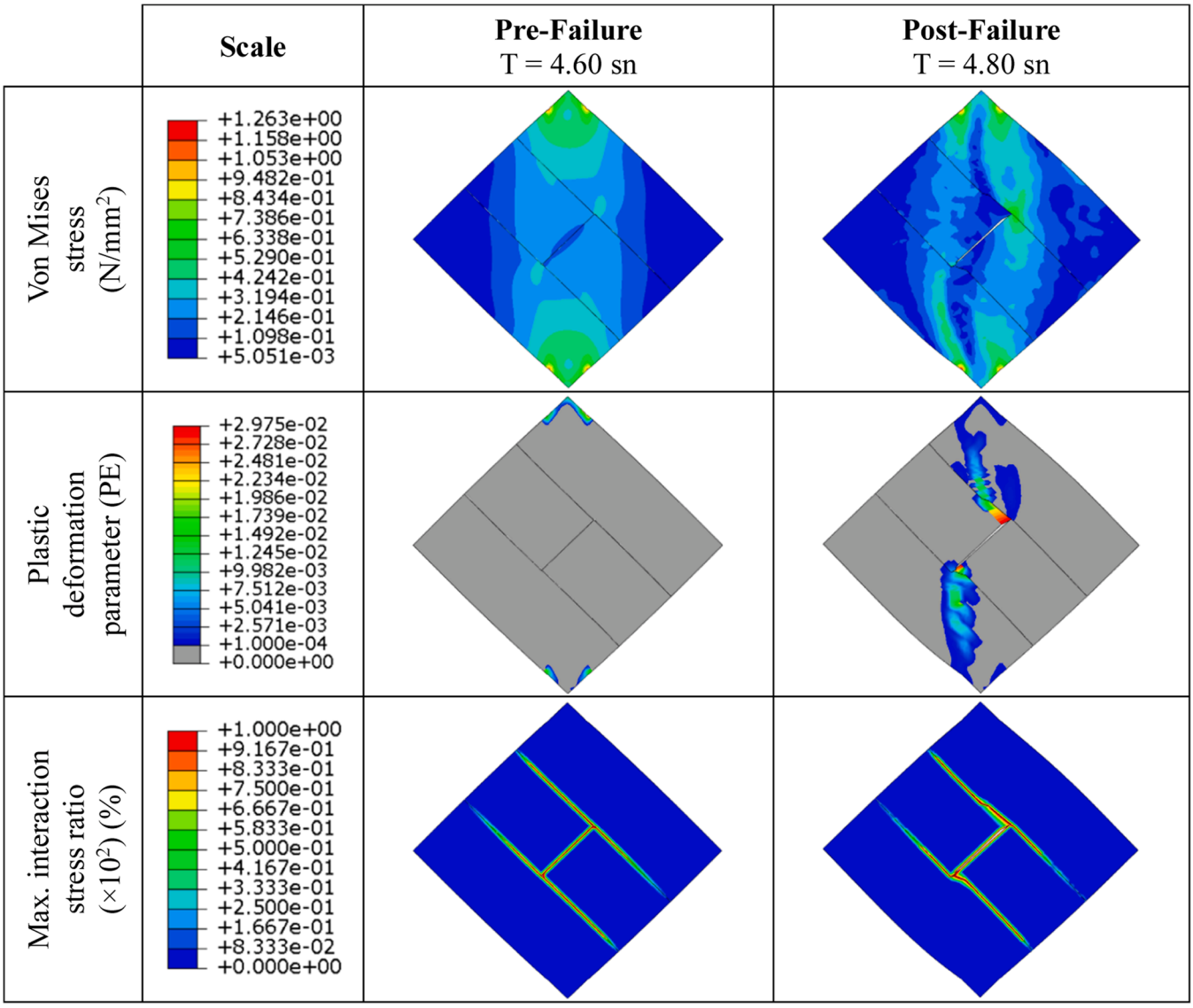


Fig. 19. Findings for the additional size 60 × 60 cm.

$$(\gamma_e)_{trd} = -3.0 \times 10^{-4}\ln(D) + 0.0026 \quad (14)$$

where $(\tau_e)_{trd}$, trend expression obtained experimentally for shear strength; $(\gamma_e)_{trd}$, trend expression obtained experimentally for shear strain; D, specimen size, respectively. The software Microsoft Excel [93] was utilized to derive logarithmic trend lines separately for the data obtained from experimental and numerical results. This software employs the Least Squares Method to perform regression analysis and generate a logarithmic trend [94,95]. To evaluate the goodness of fit between the generated curve and the data, the coefficient of determination (R^2), which ranges from 0 to 1, can be examined. R^2 values approaching 1 indicate a stronger correlation and better fit of the trend line to the observed data. The R^2 values of the trend lines are determined as: Experimental (91 % for mean, 53 % for distribution), and numerical method (98 %) (Fig. 21a,b). The trend lines were found to show good agreement with the mean shear strength data, as indicated by the high R^2 values (Fig. 21a).

The difference between the strength value obtained by writing Eq. (13) for a specimen of any size D and the strength obtained experimentally for the same specimen can be calculated. By adding this difference to the result of Eq. (13), the strength value obtained from any smaller sized specimen can be approximately determined in terms of the strength of a standard specimen of size 120 × 120 mm. In the study investigating the effect of AAC wall specimen size on shear strength, Eq. (17), which is obtained by simplifying Eqs. (15,16), was proposed to convert the shear strength obtained from smaller sized wall specimens produced using 20 cm thickness and G2 class AAC to the 120 × 120 cm specimen strength. Through Eq. (17), the shear strength for 120 × 120 cm dimensions can be obtained approximately by using the shear strength obtained experimentally (τ_{exp}) from an AAC wall specimen smaller than 120 × 120 cm dimensions as follows:

$$\tau_{120} = \left[(\tau_e)_{trd}\right]_{120} + \left\{\tau_{exp} - \left[(\tau_e)_{trd}\right]_{D_{exp}}\right\} \quad (15)$$

$$\tau_{120} = \left[-8.8 \times 10^{-2}\ln(1200) + 0.7527\right] + \left[\tau_{exp} - \left(-8.8 \times 10^{-2}\ln(D_{exp}) + 0.7527\right)\right] \quad (16)$$

$$\tau_{120} = \tau_{exp} + \left[8.8\ln(D_{exp}) - 62.4\right]10^{-2} \quad (17)$$

Here, τ_{120} is the shear strength with respect to the dimensions of 120 × 120 cm; D_{exp} and τ_{exp} are the dimension in "mm" of the specimen size smaller than 120 × 120 cm and the experimental shear strength in "MPa" obtained from this specimen, respectively. This procedure is based on the assumption that the relationship between shear strength

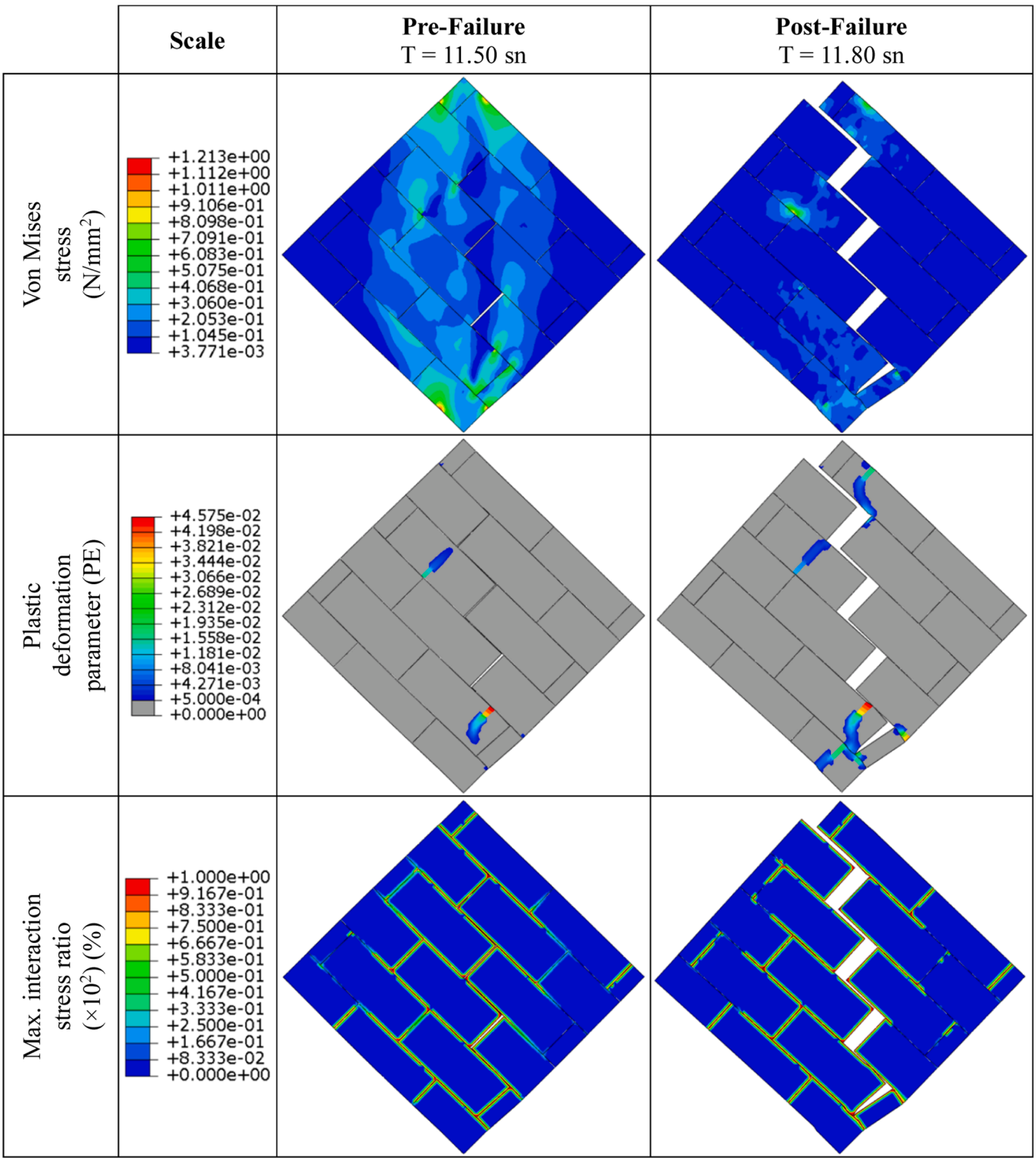


Fig. 20. Findings for the additional size 140 × 140 cm.

and specimen size has a logarithmic variation. To consider the difference between the strength of the experimentally tested specimen and the mean strength in the calculations, first; the $(\tau_e)_{trd}$ shear strength of the D_{exp} dimension specimen is calculated according to Eq. (13). This value is then subtracted from the already experimentally obtained τ_{exp} shear strength value. In this way, a difference value is obtained to be added to the shear strength value of the 120 cm specimen, which is determined by employing the trend line. Thus, the simplification of obtained Eqs. (15,16) leads to Eq. (17). It is proposed that the strength equivalent of a specimen smaller size than 120 × 120 cm, for which the shear strength τ_{exp} and specimen size D_{exp} are already known, can be obtained approximately by Eq. (17).

Based on the experimental mean shear strength values shown in Fig. 21a, the determination coefficient (R^2) obtained for the trend line given by the linear expression in Eq. (18) was determined as 95 % for mean, 56 % for distribution; and this assumption of linearity was found to be acceptable for simplification purpose. Accordingly, this study also presents Eq. (19) obtained by following similar steps above using a

Table 6
Resultant mechanical parameters for numerical modelling of specimens.

Size (cm)	Load (*P*) (kN)	($\Delta x+\Delta y$) at P_{max} (mm)	Shear strength (S_s) (MPa)	Shear strain at $(S_s)_{max}$ (γ) (mm/mm)	Shear modulus (G) (MPa)
25 × 25	13.22	0.216	0.234	0.1490 %	156.8
40 × 40	18.51	0.226	0.204	0.0976 %	209.5
50 × 50	20.49	0.241	0.181	0.0832 %	217.6
60 × 60	22.22	0.238	0.164	0.0682 %	240.1
75 × 75	25.56	0.427	0.151	0.0979 %	153.8
100 × 100	27.67	0.463	0.122	0.0797 %	153.4
120 × 120	31.38	0.557	0.116	0.0799 %	144.7
140 × 140	33.84	0.648	0.107	0.0798 %	133.9

linear trend line instead of a logarithmic curve [94,95] for experimental shear strength values (Fig. 21a), which may be more practical for engineering applications.

$$(\tau_e)_{trd} = -1.0 \times 10^{-4}\, D + 0.2947 \tag{18}$$

$$\tau_{120} = \tau_{exp} + (D_{exp} - 1200)10^{-4} \tag{19}$$

However, owing to the more inconsistent strain distribution then shear strength, and low R^2 value in the case of mean, no predictive expression for shear strain (Eq. 14) corresponding to shear strength could be established. As a result, the strain data are presented only in graphical form in Fig. 21b.

6.3. Statistical evaluation of the specimen size effect

A more comprehensive understanding of how specimen size influences shear strength behavior was pursued by employing both an exponential regression model and a one-way ANOVA [95], which were used to capture continuous trends and group-level differences, respectively. The regression model was applied to characterize the inherent relationship between specimen size and shear strength. Modeling shear strength as a function of log (size) offers a more physically meaningful and statistically robust representation of size effects observed in concrete materials, where strength typically decreases sub-linearly with increasing dimensions due to fracture mechanics, stress redistribution, and the heterogeneous nature of the material. The coefficient of determination (R^2) indicated that the regression equation explains 53 % of the variation in shear strength. The negative regression coefficient (-8.8×10^{-3}) supports the theoretical expectation of an exponential decay in shear strength with increasing specimen size (Fig. 21a). Residual diagnostics, which evaluate homoscedasticity and normality assumptions, did not reveal significant deviations, suggesting that the model is statistically well-specified on the logarithmic scale (Fig. 22).

To complement the regression analysis, a one-way ANOVA was conducted to assess whether mean shear strength values differed according to specimen size groups (25 ×25, etc.). The analysis indicated a statistically significant effect of size on shear strength $F(4,10) = 3.49$, $p = 0.049$. This result suggests that variability in stress is not solely attributable to random error but is meaningfully structured by specimen size. To determine which group pairs contributed to this overall effect, Tukey's Honestly Significant Difference (HSD) [96] test was applied. Pairwise comparisons revealed that the smallest specimen group (25 ×25) differed significantly from the largest group (120 ×120), with an adjusted p-value below 0.05 (Fig. 23). No other between-group comparisons reached statistical significance under the family-wise error rate control.

These findings support the trend observed in the regression analysis: shear strength levels in the smallest specimens are higher than those in the largest, reflecting scale-dependent attenuation. Thus, the ANOVA [95] and subsequent Tukey HSD [96] comparisons both corroborate and refine the continuous model's depiction of how specimen size influences shear strength behavior.

7. Conclusions

Although the specimen size for the diagonal shear test is required to be 120 × 120 cm according to ASTM E519 [28], smaller specimens are frequently used in literature due to reasons such as cost, workmanship, and laboratory limitations. In this study, diagonal shear strength values obtained from specimens smaller than the standard size are examined, and the results are presented in correlation with the standard. Diagonal shear strengths were obtained by producing grouted square wall specimens of five different sizes 25 × 25, 50 × 50, 75 × 75, 100 × 100, and 120 × 120 cm, using G2 class autoclaved aerated concrete (AAC) blocks with dimensions of 25 × 60 × 20 cm and constant joint thicknesses as 3 mm.

In addition to experimental work, numerical analyses were conducted to support the findings of this study. Analytical models were also developed for intermediate and large-sized specimens that could not be physically tested in conjunction with experimental cases. A simplified micro-modeling strategy was employed to replicate the corresponding experimental behavior. The experimental and numerical findings of this study are summarized as below:

- Higher diagonal shear strength values are obtained from specimens with dimensions smaller than those specified by the ASTM E519 standard. It has been seen that the mean of shear strength values increases as the specimen size becomes smaller.

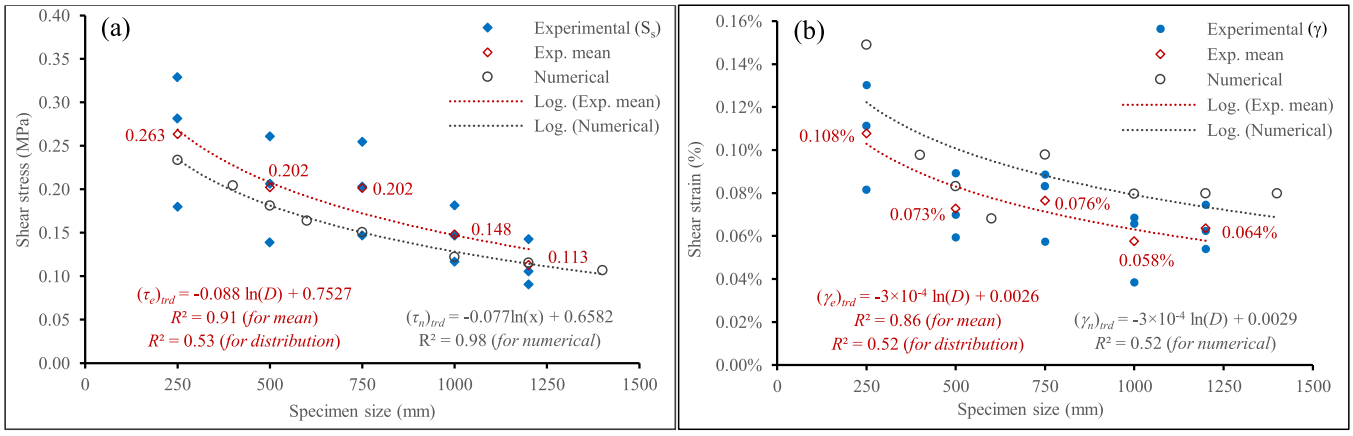


Fig. 21. (a) shear strength; (b) strain relationship with specimen size.

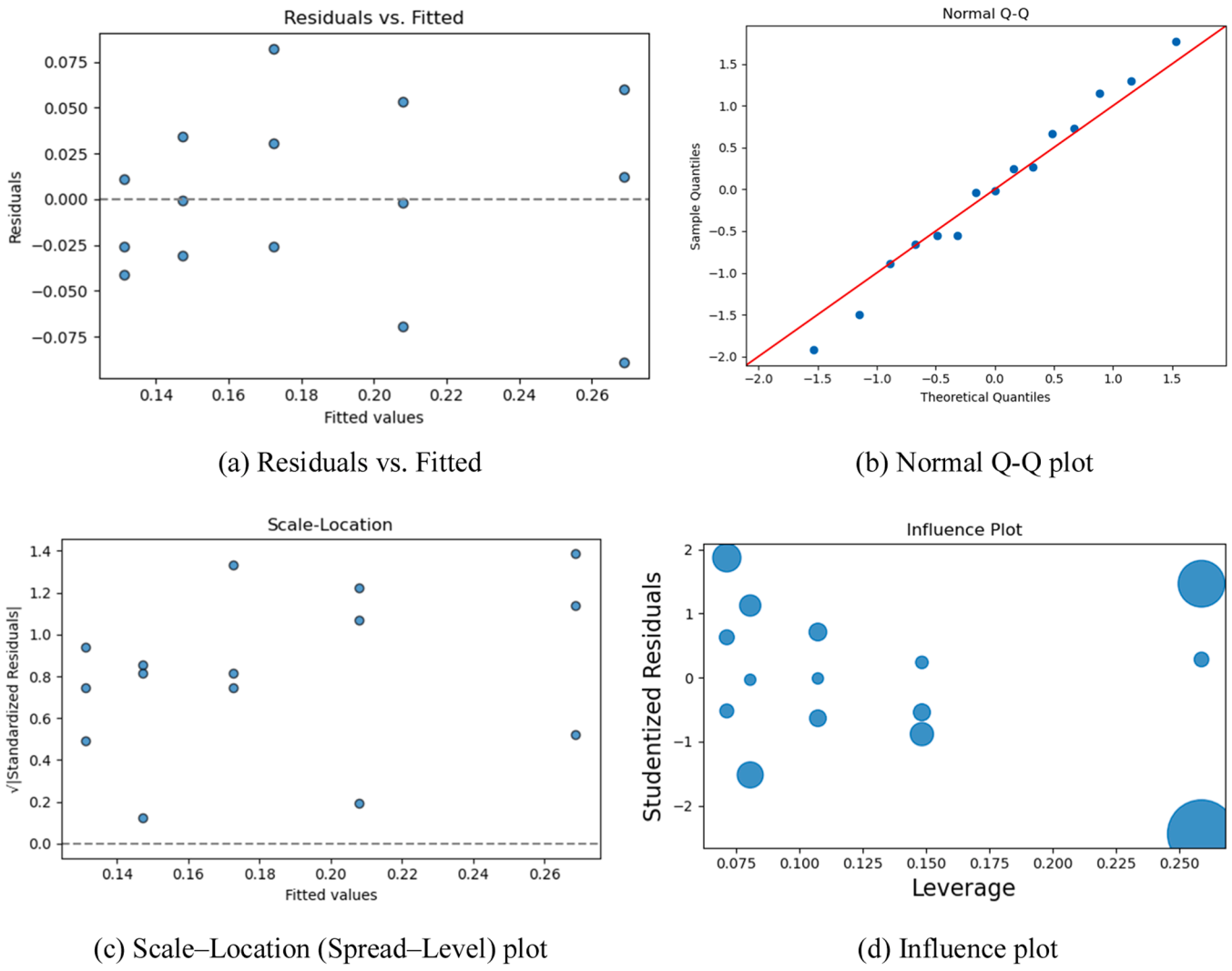


Fig. 22. Regression diagnostic plots for the Log-Transformed stress model, a) Residuals vs. Fitted plot shows the randomness of residuals; b) Normal Q–Q plot assesses the normality of residuals; c) Scale–Location plot tests for homoscedasticity; and d) Influence plot identifies high-leverage or influential observations.

- Larger specimen sizes show lower strength variability within groups, as indicated by the declining coefficient of variation (CV) values in Table 5. This reduction in strength variation may be attributed to the diminishing influence of workmanship-related inconsistencies and more uniform joint distribution on the larger wall surfaces.
- It has been observed that the workmanship factor is also effective in the arising failure mode and shear stress-strain behavior. Slightly different strength values and initial stiffness states may be observed even among specimens from the same group with nominally identical properties. It is believed that the results would become more consistent with increasing number of test specimens. As a recommendation, at least five experimental samples should be used for each group in future similar studies.
- As the specimen size increases, the fracture surface appears to be more diagonal. This behavior has been observed to result from more uniform joint distribution in large-scale specimens, caused by the presence of smaller AAC units relative to the specimen's overall size. Moreover, the failure mode was found to be more brittle when tensile fracture developed in the AAC units, rather than when failure occurred along the joints due to separation or sliding.
- Eq. (17) is proposed to convert the shear strength values obtained from experimental tests on small specimen size to the 120 × 120 cm standard specimen results. Accordingly, this study also presents Eq. (19) using a linear trend line rather than a logarithmic one, which may be more practical for engineering applications.
- The numerical results obtained exhibit good correlation with experimental findings and confirm the reliability of computer models. In this way, supportive information about the specimen size effect is also provided numerically.
- The results of statistical analysis showed that smaller specimens tend to have higher shear strength levels than larger ones, indicating a size-related decrease in strength. ANOVA [95] and Tukey HSD [96] results support this trend and confirm that specimen size affects shear strength behavior in a systematic way.

In future academic studies, more comprehensive results for AAC walls are expected to be obtained through experiments that also consider variables such as AAC class and strength, as well as the thickness of grout and plaster.

CRediT authorship contribution statement

Murat Bikçe: Writing – review & editing, Writing – original draft, Validation, Supervision, Project administration, Methodology, Investigation, Funding acquisition, Formal analysis. **Nilay Sabahoğlu:** Writing – review & editing, Resources, Methodology, Investigation, Writing – original draft, Validation, Formal analysis, Data curation,

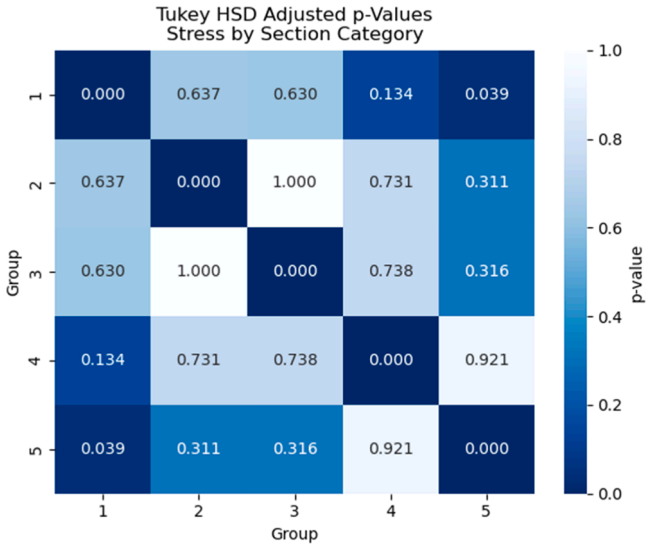


Fig. 23. Heatmap of Tukey HSD Adjusted *p*-values for pairwise comparisons of size groups. Pairwise comparisons of stress values across size groups (groups 1–5), based on Tukey's Honest Significant Difference (HSD) test. Color intensity corresponds to the magnitude of the adjusted *p*-values, with values below 0.05 (statistically significant) indicating group-level differences.

Conceptualization. **Muhammet Musab Erdem:** Writing – review & editing, Validation, Resources, Methodology, Investigation, Funding acquisition, Data curation, Writing – original draft. **Engin Emsen:** Investigation, Formal analysis, Writing – review & editing, Writing – original draft, Validation, Resources, Methodology.

Funding

The study presented in this article was carried out at İskenderun Technical University (ISTE-BTM) and Akdeniz University (AU), and was funded by the Scientific and Technological Research Council of Turkey (TÜBİTAK), under the following grant number: 118M317.

Declaration of Generative AI and AI-assisted technologies in the writing process

AI-based tools are utilized to eliminate grammatical errors and enhance the language quality, clarity, and overall readability of the text, ensuring it meets high standards of understandability.

Declaration of Competing Interest

The authors declare that they have no known competing financial interests or personal relationships that could have appeared to influence the work reported in this paper.

The author is an Editorial Board Member/Editor-in-Chief/Associate Editor/Guest Editor for this journal and was not involved in the editorial review or the decision to publish this article.

Acknowledgments

The authors would like to thank Akdeniz University, İskenderun Technical University, and Scientific and Technological Research Council of Turkey (TÜBİTAK) for their valuable support of this study. The authors also gratefully acknowledge the contribution of Dr. Münire Tuğba Aladağ (PhD), whose expertise and guidance in statistical analyses significantly improved the reliability of the results presented in this paper.

References

[1] Dolšek M, Fajfar P. The effect of masonry infills on the seismic response of a four-storey reinforced concrete frame — a deterministic assessment. Eng Struct 2008; 30:1991–2001. https://doi.org/10.1016/J.ENGSTRUCT.2008.01.001.
[2] Pujol S, Fick D. The test of a full-scale three-story RC structure with masonry infill walls. Eng Struct 2010;32:3112–21. https://doi.org/10.1016/J.ENGSTRUCT.2010.05.030.
[3] Rajeev P, Tesfamariam S. Seismic fragilities for reinforced concrete buildings with consideration of irregularities. Struct Saf 2012;39:1–13. https://doi.org/10.1016/J.STRUSAFE.2012.06.001.
[4] Fiore A, Netti A, Monaco P. The influence of masonry infill on the seismic behaviour of RC frame buildings. Eng Struct 2012;44:133–45. https://doi.org/10.1016/J.ENGSTRUCT.2012.05.023.
[5] Korkmaz KA, Kayhan AH, Ucar T. Seismic assessment of R/C residential buildings with infill walls in Turkey. Comput Concr 2013;12. https://doi.org/10.12989/cac.2013.12.5.681.
[6] Mondal G, Tesfamariam S. Effects of vertical irregularity and thickness of unreinforced masonry infill on the robustness of RC framed buildings. Earthq Eng Struct Dyn 2014;43. https://doi.org/10.1002/eqe.2338.
[7] Ganesan N, Indira PV, Irshad P. RCC frames with ferrocement and fiber reinforced concrete infill panels under reverse cyclic loading. Adv Concr Constr 2017;5. https://doi.org/10.12989/acc.2017.5.3.257.
[8] Benavent-Climent A, Ramírez-Márquez A, Pujol S. Seismic strengthening of low-rise reinforced concrete frame structures with masonry infill walls: Shaking-table test. Eng Struct 2018;165. https://doi.org/10.1016/j.engstruct.2018.03.026.
[9] Dilmac H, Ulutas H, Tekeli H, Demir F. The investigation of seismic performance of existing RC buildings with and without infill walls. Comput Concr 2018;22. https://doi.org/10.12989/cac.2018.22.5.439.
[10] Binici B, Canbay E, Aldemir A, Demirel IO, Uzgan U, Eryurtlu Z, et al. Seismic behavior and improvement of autoclaved aerated concrete infill walls. Eng Struct 2019;193. https://doi.org/10.1016/j.engstruct.2019.05.032.
[11] Onat O. Experimental damage evaluation of prototype infill wall based on forced vibration test. Adv Concr Constr 2019;8. https://doi.org/10.12989/acc.2019.8.2.077.
[12] Wijaya H, Rajeev P, Gad E, Amirsardari A. Effect of Infill-Wall material types and modeling techniques on the seismic response of reinforced concrete buildings. Nat Hazards Rev 2020;21. https://doi.org/10.1061/(asce)nh.1527-6996.0000395.
[13] Bikçe M, Emsen E, Erdem MM, Bayrak OF. An investigation on behavior of RC frames with non-interacting infill wall. Eng Struct 2021;245. https://doi.org/10.1016/j.engstruct.2021.112920.
[14] Erdem MM, Emsen E, Bikçe M. Experimental and numerical investigation of new flexible connection elements between infill walls-RC frames. Constr Build Mater 2021;296:123605. https://doi.org/10.1016/J.CONBUILDMAT.2021.123605.
[15] Kasapgil SM, Binici B, Canbay E. Seismic behavior of AAC infill walls insulated with cementitious lightweight panels in reinforced concrete frames. Eng Struct 2021;248. https://doi.org/10.1016/j.engstruct.2021.113215.
[16] Wang F, Zhao K, Zhang J, Yan K. Influence of different types of infill walls on the hysteretic performance of reinforced concrete frames. Buildings 2021;11. https://doi.org/10.3390/buildings11070310.
[17] Dorji S, Derakhshan H, Thambiratnam DP. Experimental investigation of semi-interlocking mortarless masonry-infilled frames. Structures 2022;43. https://doi.org/10.1016/j.istruc.2022.07.004.
[18] Gupta A, Meena GK, Singhal V. Strengthening of autoclaved aerated concrete (AAC) masonry wallettes with fabric reinforced cementitious matrix for in-plane shear and out-of-plane loads. Structures 2023;51. https://doi.org/10.1016/j.istruc.2023.03.099.
[19] Shi M, Choi Y, Kang S. A study of the infill wall of the RC frame using a quasi-static pushover analysis. Comput Concr 2023;32. https://doi.org/10.12989/cac.2023.32.5.455.
[20] Sleiman E, Ferrier E, Michel L, Saidi M. Seismic behavior of masonry-infilled reinforced concrete frames strengthened using ultra-high performance concrete diagonal strips. Structures 2024;59. https://doi.org/10.1016/j.istruc.2023.105790.
[21] Zhang J, Guo X, Tang X. A L. Experimental and numerical simulation of seismic behavior of reinforced concrete frames infilled with refractory straw blocks. Structures 2024;69:107475. https://doi.org/10.1016/J.ISTRUC.2024.107475.
[22] Zhang J, A L, Guo X, Xu Z. Seismic vulnerability assessment of reinforced concrete school buildings based on the concept of balanced seismic shear force distribution. Structures 2025;71:108184. https://doi.org/10.1016/J.ISTRUC.2024.108184.
[23] Perrone D, Leone M, Aiello MA. Evaluation of the infill influence on the elastic period of existing RC frames. Eng Struct 2016;123. https://doi.org/10.1016/j.engstruct.2016.05.050.
[24] Alecci V, Fagone M, Rotunno T, De Stefano M. Shear strength of brick masonry walls assembled with different types of mortar. Constr Build Mater 2013;40. https://doi.org/10.1016/j.conbuildmat.2012.11.107.
[25] Ferretti D, Michelini E, Rosati G. Mechanical characterization of autoclaved aerated concrete masonry subjected to in-plane loading: experimental investigation and FE modeling. Constr Build Mater 2015;98. https://doi.org/10.1016/j.conbuildmat.2015.08.121.
[26] Mehrabi AB, Benson Shing P, Schuller MP, Noland JL. Experimental evaluation of Masonry-Infilled RC frames. J Struct Eng 1996;122. https://doi.org/10.1061/(asce)0733-9445(1996)122:3(228).
[27] Basha SH, Kaushik HB. Evaluation of nonlinear material properties of Fly ash brick masonry under compression and shear. J Mater Civ Eng 2015;27. https://doi.org/10.1061/(asce)mt.1943-5533.0001188.

[28] ASTM E519/E519M. Test method for diagonal tension (Shear) in masonry assemblages. West Conshohocken, PA: ASTM International; 2022. https://doi.org/10.1520/E0519_E0519M-22.
[29] Segura J, Pelà L, Saloustros S, Roca P. Experimental and numerical insights on the diagonal compression test for the shear characterisation of masonry. Constr Build Mater 2021;287. https://doi.org/10.1016/j.conbuildmat.2021.122964.
[30] Ghanem G, Sheirf A, Honsy H. Suggested modifications to the diagonal tension test calculation for masonry assemblages. 10th Int Brick/Block Mason Conf 1994.
[31] Rosti A, Penna A, Rota M, Magenes G. In-plane cyclic response of low-density AAC URM walls. Mater Struct/Mater Et Constr 2016;49. https://doi.org/10.1617/s11527-016-0825-5.
[32] Ismail N, El-Maaddawy T, Najmal A, Khattak N. Experimental in-plane performance of insulated concrete and brick masonry wall panels retrofitted using polymer composites. Bull NZ Soc Earthq Eng 2018;51. https://doi.org/10.5459/bnzsee.51.2.85-91.
[33] Mezrea PE, Ispir M, Balci IA, Bal IE, Ilki A. Diagonal tensile tests on historical brick masonry wallets strengthened with fabric reinforced cementitious mortar. Structures 2021;33. https://doi.org/10.1016/j.istruc.2021.04.076.
[34] Michelini E, Cerioni R, Riva A, Boretti G, Casillo A, Ferretti D. Experimental characterization of AAC masonry in shear: effect of block density, mortar, and test setup. Ce/Pap 2023;6. https://doi.org/10.1002/cepa.2160.
[35] Badonbok Lyngkhoi R, Warjri T, Bennett S, Marthong C. Effect of moisture content on the mechanical behaviour of AAC masonry systems. Mater Today Proc 2023. https://doi.org/10.1016/j.matpr.2023.03.778.
[36] Raavi SSD, Tripura DD. Compressive and shear behavior of cement stabilized rammed earth wallettes reinforced with coir, bamboo splints and steel bars. Structures 2023;53. https://doi.org/10.1016/j.istruc.2023.05.005.
[37] Demaj A, Gago A, Marques AI, Gomes Ferreira J. Shear performance of brick masonry walls reinforced with twisted steel bars. Structures 2023;58. https://doi.org/10.1016/j.istruc.2023.105579.
[38] Latha L, Ray-Chaudhuri S, Mukhopadhyay S, Bajpai KK. Seismic performance enhancement of unreinforced brick masonry buildings by retrofitting with reinforced concrete bands: full scale experiments. J Struct Eng 2022;148. https://doi.org/10.1061/(asce)st.1943-541x.0003460.
[39] Vailati M, Mercuri M, Gregori A. One-head masonry panels reinforced with industrial-waste fiber reinforced mortar: investigating the effect of bed joints and coating reinforcement in the diagonal compressive behavior. Structures 2024;63:106474. https://doi.org/10.1016/J.ISTRUC.2024.106474.
[40] Baeen SB, Dharek MS, Raghunath S, Vinay S, Kishor VS, Aejaz M. Effect of thin reinforcement in bed-joint on the compressive and shear strength of brick and block masonry- an experimental investigation. J Build Pathol Rehabil 2025;10. https://doi.org/10.1007/s41024-025-00567-y.
[41] Lim WY. Failure mode dependent shear strength of unreinforced concrete brick masonry wall panels. Constr Build Mater 2024;414. https://doi.org/10.1016/j.conbuildmat.2024.134976.
[42] Kanchidurai S, Krishanan PA, Baskar K, Mohan KSR. Strength characteristic of novel mesh embedment technique for new brick construction with least expensive material. Eng Struct 2019;178. https://doi.org/10.1016/j.engstruct.2018.10.062.
[43] Kubica J, Galman I. Comparison of two ways of AAC block masonry strengthening using CFRP strips - diagonal compression test. Procedia Eng 2017;193. https://doi.org/10.1016/j.proeng.2017.06.184.
[44] Silva LM, Vasconcelos G, Lourenço PB. Innovative systems for earthquake-resistant masonry infill walls: characterization of materials and masonry assemblages. J Build Eng 2021;39. https://doi.org/10.1016/j.jobe.2021.102195.
[45] Yardim Y, Lalaj O. Shear strengthening of unreinforced masonry wall with different fiber reinforced mortar jacketing. Constr Build Mater 2016;102. https://doi.org/10.1016/j.conbuildmat.2015.10.095.
[46] Ozsayin B, Yilmaz E, Ispir M, Ozkaynak H, Yuksel E, Ilki A. Characteristics of CFRP retrofitted hollow brick infill walls of reinforced concrete frames. Constr Build Mater 2011;25. https://doi.org/10.1016/j.conbuildmat.2011.04.036.
[47] Thatikonda NP, Baraldi D, Boscato G, Cecchi A. Specimen size sensitivity on diagonal compression tests for masonry. Multiscale and Multiphysics Modelling for Advanced and Sustainable Materials. Advanced Structured Materials, 231. Cham: Springer; 2025. p. 405–16. https://doi.org/10.1007/978-3-031-84379-2_30.
[48] Lim WY. Experimental investigation of size effect on unreinforced concrete brick masonry walls under in-plane shear loading. Constr Build Mater 2024;428. https://doi.org/10.1016/j.conbuildmat.2024.136346.
[49] Penna A, Mandirola M, Rota M, Magenes G. Experimental assessment of the in-plane lateral capacity of autoclaved aerated concrete (AAC) masonry walls with flat-truss bed-joint reinforcement. Constr Build Mater 2015;82. https://doi.org/10.1016/j.conbuildmat.2015.02.057.
[50] Jasiński R, Drobiec Ł. Study of autoclaved aerated concrete masonry walls with horizontal reinforcement under compression and shear. Procedia Eng 2016;161. https://doi.org/10.1016/j.proeng.2016.08.758.
[51] Asadzadeh SA, Mohammadi M, K. A. Attari N, Zareei SA. An experimental study on finding prequalified connectors between the wall and steel frame infilled with Autoclave-Cured aerated concrete blocks. J Earthq Eng 2022;26. https://doi.org/10.1080/13632469.2020.1822231.
[52] Xu C, Nehdi ML, Wang K, Guo Y. Experimental study on seismic behavior of novel AAC prefabricated panel walls. J Build Eng 2021;44. https://doi.org/10.1016/j.jobe.2021.103390.
[53] Aydin BB, Binici B, Hendriks MAN, Tuncay K. Lattice modeling and testing of aerated autoclaved concrete infilled frames. Eng Struct 2022;251. https://doi.org/10.1016/j.engstruct.2021.113467.
[54] Kałuża M. AAC-block walls with surface application of non-structural plastering materials as newly configured and improved structures subjected to diagonal compression. ThinWalled Struct 2024;195. https://doi.org/10.1016/j.tws.2023.111459.
[55] Malomo D, Pulatsu B. Discontinuum models for the structural and seismic assessment of unreinforced masonry structures: a critical appraisal. Structures 2024;62. https://doi.org/10.1016/j.istruc.2024.106108.
[56] ASTM C1019-20. Standard test method for sampling and testing, grout for masonry. West Conshohocken, PA: ASTM International; 2020. https://doi.org/10.1520/C1019-20.
[57] Narayanan N, Ramamurthy K. Structure and properties of aerated concrete: a review. Cem Concr Compos 2000;22. https://doi.org/10.1016/S0958-9465(00)00016-0.
[58] Michelini E, Ferretti D, Miccoli L, Parisi F. Autoclaved aerated concrete masonry for energy efficient buildings: state of the art and future developments. Constr Build Mater 2023;402. https://doi.org/10.1016/j.conbuildmat.2023.132996.
[59] CEB Bulletins. Manual of Autoclaved Aerated Concrete Design and Technology, 122. Lausanne, Switzerland: International Federation for Structural Concrete (FIB); 1977.
[60] Lourenço P.B. Computational strategies for masonry structures. 1996.
[61] Lourenço PB, Pina-Henriques J. Validation of analytical and continuum numerical methods for estimating the compressive strength of masonry. Comput Struct 2006;84. https://doi.org/10.1016/j.compstruc.2006.08.009.
[62] Greco F, Leonetti L, Luciano R, Pascuzzo A, Ronchei C. A detailed micro-model for brick masonry structures based on a diffuse cohesive-frictional interface fracture approach. Procedia Struct Integr 2020;25. https://doi.org/10.1016/j.prostr.2020.04.038.
[63] Lourenço PB, Rots JG. Multisurface interface model for analysis of masonry structures. J Eng Mech 1997;123. https://doi.org/10.1061/(asce)0733-9399(1997)123:7(660).
[64] Page AW. Finite element model for masonry. ASCE J Struct Div 1978;104. https://doi.org/10.1061/jsdeag.0004969.
[65] Arya SK, Hegemier GA. Finite element method for interface problems. ASCE J Struct Div 1982;108. https://doi.org/10.1061/jsdeag.0005874.
[66] Lotfi HR, Shing PB. Interface model applied to fracture of masonry structures. J Struct Eng 1994;120. https://doi.org/10.1061/(asce)0733-9445(1994)120:1(63).
[67] Kumar N, Amirtham R, Pandey M. Plasticity based approach for failure modelling of unreinforced masonry. Eng Struct 2014;80. https://doi.org/10.1016/j.engstruct.2014.08.021.
[68] Oliveira DV, Lourenço PB. Implementation and validation of a constitutive model for the cyclic behaviour of interface elements. Comput Struct 2004;82. https://doi.org/10.1016/j.compstruc.2004.03.041.
[69] D'Altri AM, de Miranda S, Castellazzi G, Sarhosis V. A 3D detailed micro-model for the in-plane and out-of-plane numerical analysis of masonry panels. Comput Struct 2018;206. https://doi.org/10.1016/j.compstruc.2018.06.007.
[70] Lubliner J, Oliver J, Oller S, Oñate E. A plastic-damage model for concrete. Int J Solids Struct 1989;25. https://doi.org/10.1016/0020-7683(89)90050-4.
[71] Lee J, Fenves GL. Plastic-Damage model for cyclic loading of concrete structures. J Eng Mech 1998;124. https://doi.org/10.1061/(asce)0733-9399(1998)124:8(892).
[72] Earij A, Alfano G, Cashell K, Zhou X. Nonlinear three–dimensional finite–element modelling of reinforced–concrete beams: computational challenges and experimental validation. Eng Fail Anal 2017;82. https://doi.org/10.1016/j.engfailanal.2017.08.025.
[73] Labibzadeh M, Zakeri M, Shoaib AA. A new method for CDP input parameter identification of the ABAQUS software guaranteeing uniqueness and precision. Int J Struct Integr 2017;8. https://doi.org/10.1108/IJSI-03-2016-0010.
[74] Alam Z, Sun L, Zhang C, Su Z, Samali B. Experimental and numerical investigation on the complex behaviour of the localised seismic response in a multi-storey plan-asymmetric structure. Struct Infrastruct Eng 2021;17. https://doi.org/10.1080/15732479.2020.1730914.
[75] Nana WSA, Bui TT, Limam A, Abouri S. Experimental and numerical modelling of shear behaviour of Full-scale RC slabs under concentrated loads. Structures 2017;10. https://doi.org/10.1016/j.istruc.2017.02.004.
[76] Dassault Systèmes. Abaqus Unified FEA - SIMULIA™ by Dassault Systèmes®. Dassault Systèmes Simulia 2021.
[77] Carreira DJ, Chu KH. Stress-strain relationship for plain concrete in compression. J Am Concr Inst 1985;82. https://doi.org/10.14359/10390.
[78] Elkady A. ABAQUS CDP Generator: A tool for generating ABAQUS input data for the Concrete Damage Plasticity (CDP) material model. 2024. doi:10.5281/zenodo.7755925.
[79] BSI Standards Publication. EN 1996-1-1: Eurocode 6: design of masonry structures - Part 1-1: general rules for reinforced and unreinforced masonry structures. Brussels: European Committee for Standardization; 2005.
[80] Abdulla KF, Cunningham LS, Gillie M. Simulating masonry wall behaviour using a simplified micro-model approach. Eng Struct 2017;151. https://doi.org/10.1016/j.engstruct.2017.08.021.
[81] Ortega J, Mendes N, Vasconcelos G. Numerical simulation of the Tension–Compression behavior of tie connections in brick masonry walls. CivilEng 2022;3. https://doi.org/10.3390/civileng3020026.
[82] Campilho RDSG, de Moura MFSF, Domingues JJMS. Using a cohesive damage model to predict the tensile behaviour of CFRP single-strap repairs. Int J Solids Struct 2008;45. https://doi.org/10.1016/j.ijsolstr.2007.10.003.
[83] Bolhassani M, Hamid AA, Lau ACW, Moon F. Simplified micro modeling of partially grouted masonry assemblages. Constr Build Mater 2015;83. https://doi.org/10.1016/j.conbuildmat.2015.03.021.

[84] Bhosale A, Zade NP, Davis R, Sarkar P. Experimental investigation of autoclaved aerated concrete masonry. J Mater Civ Eng 2019;31. https://doi.org/10.1061/(asce)mt.1943-5533.0002762.
[85] Zhang S, Richart N, Beyer K. Numerical evaluation of test setups for determining the shear strength of masonry. Mater Struct/Mater Et Constr 2018;51. https://doi.org/10.1617/s11527-018-1236-6.
[86] Miccoli L, Ferretti D, Michelini E, Loderer F. Determination of the initial shear strength of AAC masonry with and without pre-compression according to EN 1052-3. Ce/Pap 2023;6. https://doi.org/10.1002/cepa.2220.
[87] Benzeggagh ML, Kenane M. Measurement of mixed-mode delamination fracture toughness of unidirectional glass/epoxy composites with mixed-mode bending apparatus. Compos Sci Technol 1996;56. https://doi.org/10.1016/0266-3538(96)00005-X.
[88] Camanho P, Davila CG. Mixed-Mode decohesion finite elements in for the simulation composite of delamination materials. Nasa 2002. TM-2002-21.
[89] Michelini E, Ferretti D, Pizzati M. The influence of density on the fracture energy of AAC: from experimental investigation to the calibration of a cohesive law. Constr Build Mater 2023;400. https://doi.org/10.1016/j.conbuildmat.2023.132547.
[90] Debnath P, Dutta SC, Halder L, Choubey B. Lateral behaviour of unreinforced masonry walls with different sizes and locations of opening and effect of strengthening measures: a computational approach. Bull Earthq Eng 2024;22. https://doi.org/10.1007/s10518-023-01798-5.
[91] Bažant ZP. Size effect in blunt fracture: concrete, rock, metal. J Eng Mech 1984;110. https://doi.org/10.1061/(asce)0733-9399(1984)110:4(518).
[92] FEMA 306. Evaluation of earthquake damaged concrete and masonry wall buildings. Washington, DC: FEMA; 1998.
[93] Microsoft Corporation. Microsoft Excel – spreadsheet software. MicrosoftCom 2014.
[94] Draper NR, Smith H. Applied regression analysis. Third Edition 2014. https://doi.org/10.1002/9781118625590.
[95] Kutner M, Nachtsheim C, Neter J, Li W. Applied statistical linear models. Fifth edition. New York, NY, USA: McGraw-Hill Irwin; 2005.
[96] Tukey JW. Comparing individual means in the analysis of variance. Biometrics 1949;5. https://doi.org/10.2307/3001913.